A FE parametric study of RWS beam-to-column bolted connections with cellular beams

Konstantinos Daniel Tsavdaridis [a],*, Theodore Papadopoulos [b]

[a] *Institute for Resilient Infrastructure, School of Civil Engineering, University of Leeds, LS2 9JT, Leeds, UK*
[b] *Pell Frischmann Consultants, 5 Manchester Square, W1U 3PD, London, UK*

ABSTRACT

In recent years, researchers study alternative connection designs for steel seismic-resistant frames by reducing the beam section in different ways including that of creating an opening in its web (RWS connections). A similar design is applied in the fabrication of perforated (i.e. cellular and castellated) beams mostly used to support the service integration, as well as the significant mass reduction in steel frames.
This paper presents a comprehensive finite element (FE) analysis of extended end-plate beam-to-column connections, with both single and multiple circular web openings introduced along the length of the beam while subjected to the cyclic loading proposed by the SAC protocol from FEMA 350 (2000). The three-dimensional (3D) FE solid model was validated against FE and experimental results and the chosen configuration was capable of representing the structural behaviour of a partially restrained connection, without the necessity to be idealised as fully fixed. The study focuses in the interaction of such connections and the mobilisation of stresses from the column to the perforated beam. The parameters introduced were the distance from the face of the column, S, and the web opening spacing, S_o, with closely and widely spaced web openings. It is found that RWS connections with cellular beams behave in a satisfactory manner and provide enhanced performance in terms of the stress distribution when subjected to cyclic loading. The design of partially restrained RWS connections should be primarily based on the distance of the first opening from the face of the column.

1. Introduction

In the past, fully welded connections were considered to provide the optimum combination of strength, stiffness and ductility which according to codes are the major factors in the seismic-resistant design of connections (Eurocode 3 and Eurocode 8) [1,2]. However, both the 1994 Northridge and 1995 Kobe earthquakes had destructive effects and proved that welded steel moment frames were generally prone to premature brittle failure. This was an area of great concern for engineers since, in particular for the 1994 Northridge earthquake; there was great damage for what was regarded as being a moderate event with a 6.8 Richter scale magnitude and duration of ground motion shaking of about 10 s. Brittle damage was generally confined to the vicinity of welds of beam-to-column connections and had occurred in older and low-rise as well as new and high-rise buildings. Studies were conducted by the Federal Emergency Management Agency (FEMA) and the SAC Joint Venture resulting reports ranging

from FEMA 350 [3] to 355F with main aim to develop reliable, practical and cost-effective design guidelines, specifications and standards of practice in order to reduce the seismic hazards of steel moment-frame structures.

Inadequate workmanship which led to the poor quality of welds was first believed to be the only cause for the brittle damage. Test results by SAC on all pre-Northridge connections indicated that an even improved workmanship was in most cases insufficient by itself to achieve reliable performance. This led to the conclusion that connections were not well understood, with many factors contributing to their inadequate performance. Pre-Northridge connections had drawbacks mainly related to their geometry with large stress concentrations occurring in the critical zone where the beam joins the column. This phenomenon made them susceptible to fracture in a brittle manner before yielding occurred, while forming a plastic hinge in the beam very close to the connection, as most of the seismic energy was absorbed by the connection, which resulted in low rotational ductility under cyclic loading. Alternative solutions were considered ([2,3]: Part 3) by reinforcing connections or having a Reduced Beam Section (RBS) type of connection as shown in Fig. 1 in order to achieve the "*weak beam-strong column*" mechanism illustrated in Fig. 2 which enables the development of an internal plastic hinge within the beam acting

* Corresponding author.
E-mail addresses: k.tsavdaridis@leeds.ac.uk, k.tsavdaridis@leeds.ac.uk
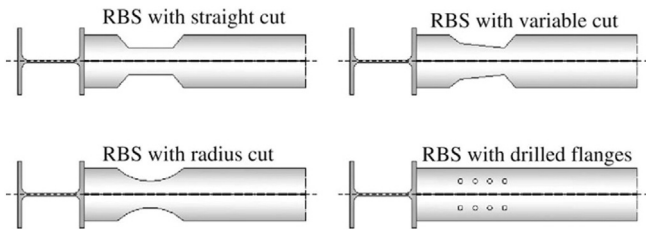(K.D. Tsavdaridis).

Fig. 1. Shapes of Reduced Beam Sections [4].

as a ductile seismic design while attracting high stresses and allowing beam rotations.

In contrast, extensive investigations undertaken since 1994 on bolted connections with extended end-plates have shown that adequate energy can be dissipated without a substantial loss of strength, making such connections suitable to replace the welded ones [5–7].

RBS, otherwise known as "Dogbone" connections can have different forms produced by alternative cuts to locally reduce the cross-sectional area of the beams and achieve material efficiency. This seismic-resistant design of connections falls within the concept of performance-based design. Popov et al. [6] studied the pre-Northridge connections, analysed their brittle failure and proposed two remedy designs using either a Dogbone or reinforcing plates. Research by Lee and Kim [8] and Pachoumis et al. [4] also exhibited satisfactory levels of connection ductility with the plastic hinge forming at the RBS area without fracture being developed. Recently, the concept of merging the purposely weakened connections with the use of perforated beams was investigated, as a trend of achieving material efficiency and considering material reduction through beam web cuts, also known as Reduced Web Section (RWS). However, limited research has been conducted up to date regarding further understanding and the design limitations of connections when perforated beams with standard isolated web openings [9–11] and non-standard isolated web openings [12,13] are used. Perforated beams offer numerous advantages depending on their manufacturing procedure (either zig-zag profile cutting process or plate assembly technique with web cut-outs), as they can span longer without the increase in weight, hence with a reduced material volume while maintaining their bending capacity. They can also integrate services within the floor-to-ceiling zone of the structure, gaining extra space with great economic impact. There has been a lot of research on perforated beam webs carried out by many researchers with the geometry of the perforations ranging from circular, hexagonal, to even elliptically-based shapes [14–17]. This leads to the current study which will focus on the use of cellular beams (i.e. perforated beams with a series of circular web openings along the length of the beam) to beam-to-column connections. In this way, the stress distribution in the vicinity of the web openings and the level of interaction between the critical failure modes (i.e. web-post buckling and Vierendeel mechanism) associated to perforated beams — so far only designed by the

industry and manufactures as simply supported beams — and the ones related to such partially restrained connections. Full 3D FE discretized models are employed to assess their hysteretic performance.

2. Reduced Web Sections (RWS)

Research undertaken in RWS is related to their fabrication process (increased cost due to the web cutting and perhaps the welding of the section), buckling issues (stability issues due to the increased depth in certain cases), number of web openings, as well as their use in steel MRFs.

It has been proved [13,18,19] that RWS connections provide a higher rotational capacity of the order of 0.05 rad, and [12] recommends a minimum of 0.04 rad, whilst 0.035 rad is suggested by [2,3] to be acceptable in seismic design. On the other hand, the local shear capacity of the beams is decreased because of the opening existence. In parallel, researches considering the progressive collapse scenarios of MRFs have suggested that the catenary behaviour of steel framing, rather than its flexural action only, should be assessed in order to redistribute the loads and resist further collapse in seismic as well as blast-resistant designs [20]. Therefore, nowadays' trend is to increase the rotational capacity of connections from what was suggested by post-Northridge codes, as the catenary action was not considered and resulted in the design of connections being incapable of large inelastic rotations.

Further research was conducted for the seismic-resistant design of steel MRFs using beams with isolated web openings by [11]. Both experimental and numerical analyses performed were subjected to pseudo-dynamic, quasi-static and push-over actions. Strong emphasis was put in analysing the failure modes and avoiding brittle fracture. The comparison with typical beam-to-column connections (without web openings) as well as with connections consisting of any of the three different sizes of circular web openings was established. The results revealed a ductile failure of the frame with adequate stiffness which was not weakened significantly by the web openings. The focus on the beam-to-column connection helped in developing the Vierendeel mechanism in the beam without brittle web fracture. The Vierendeel mechanism is a ductile failure mode with the formation of four plastic hinges around the edge of the web opening with the redistribution of the load in the vicinity of the opening, while the vertical shear forces are transferred from the top to the bottom tee-section.

Little difference was observed in the failure modes of the four specimens examined (opening sizes of 90 mm and 100 mm; opening locations of 250 mm and 300 mm). An additional case study with a push-over analysis of a 17-storey MRF which had undergone damage in the Northridge earthquake was conducted and concluded that no brittle damage has occurred but the creation of plastic hinges in the weakened areas. The results demonstrated the advances of using RWS connections in the design of MRFs, hence the need for further research on various types of connections. Hence, it is deemed necessary to investigate connections with different web opening shapes, sizes, location (if a single opening) and number of penetrations. Since 2009, limited research
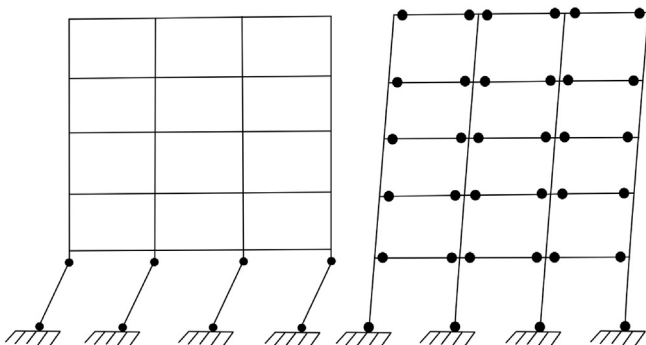

Fig. 2. First soft-storey failure against "*weak beam-strong column*" mechanism.

Table 1
Dimensions of the connection (all in mm and mm²).

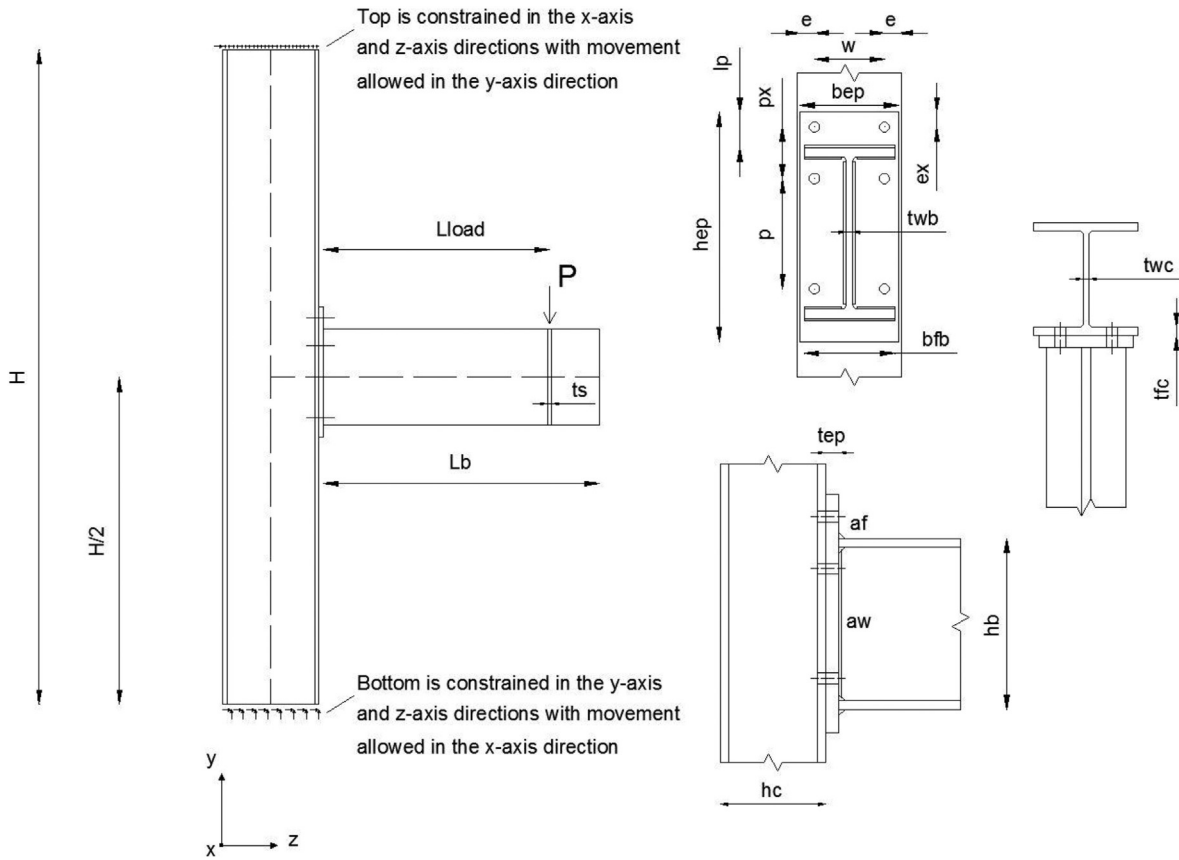| Beam (IPE300)		End-plate		Column (HE160B)		Bolt (M20)		Load and stiffener		Weld throat thicknesses	
b_{fb}	150.9	l_p	70.0	b_{fc}	160.1	A_s	245.0	L_{load}	1250.0	a_f	6.0
h_b	298.9	b_{ep}	150.0	h_c	162.5	d_o	20.0	t_s	10.8	a_w	4.0
L_b	1550.0	h_{ep}	380.0	H	3625.0	d_{hb}, d_{nb}	32.0				
t_{fb}	10.8	t_{ep}	20.0	t_{fc}	12.6	e, e_x	30.0				
t_{wb}	7.3			t_{wc}	8.5	p	200.0				
						p_x	90.0				
						t_{hb}	12.5				
						t_{nb}	18.0				
						w_p	90.0				

Fig. 3. Detailed configuration of the extended end-plate connection [22].

has been carried out on RWS connections, and the comparisons against the advances gained from the RBS connections remain unanswered.

The structural performance of such RWS semi-rigid connection type with the use of a series of web openings and typical cellular beams, instead of only one local reduction at the cross-sectional area of the beam, has not yet been examined under cyclic loading. Consequently, the aim of the work is to check the suitability of cellular beams to perform in seismic situations by examining the energy dissipation, the mobilisation of stresses away from the connection, and the hysteretic behaviour of RWS connections, as well as to identify the critical geometric parameters of such connections supporting their widespread design and promoting the practical use of perforated steel beams in MRFs. This research will study the behaviour of partially restrained bolted RWS beam-to-column connections under cyclic loading. The effect of various geometric parameters such as the distance from the face of the column, S, and the web opening spacing, S_o, were assessed while large circular web openings of diameter, d_o, equal to 0.8 h were used throughout, and the results were scrutinised in order to propose alternative optimum structural designs. The potential of adding a series of closely as well as widely spaced web openings along the length of the beam was also examined.

3. Moment connections

Traditional approaches to steel frame design assume the connections to be either pinned or fully rigid. This simplifies the analysis and design procedures but the predicted response may not be ideal since in practice most connections transmit some moments and experience some rotations. The term 'semi-rigid' is nowadays commonly used to designate connections between these two extremes. The American Institute of Steel Construction (AISC) usually separates connections into full strength or partial strength based on their capability to transfer the full plastic moment of the framing beams, and into full restraint (FR), partial restraint (PR) or pinned for what concerns their stiffness. The connection can either be brittle or ductile and used in ordinary
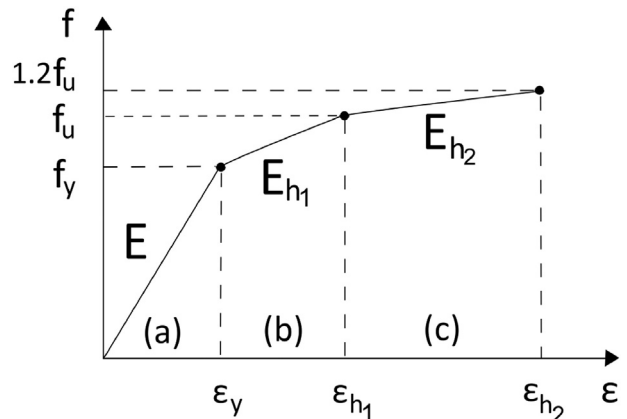
Table 2
Mechanical properties of the connection (all in MPa).

Beam		End-plate		Column		Bolt		Load stiffener		Weld	
$f_{u,beam}$	445.0	$f_{u,ep}$	463.4	$f_{u,c}$	422.2	$f_{u,b}$	1000.0	$f_{u,s}$	443.0	$f_{u,w}$	463.4
$f_{y,beam}$	308.5	$f_{y,ep}$	291.5	$f_{y,c}$	289.4	$f_{y,b}$	900.0	$f_{y,s}$	314.0	$f_{y,w}$	291.5

Fig. 4. Material tri-linear stress–strain curve.
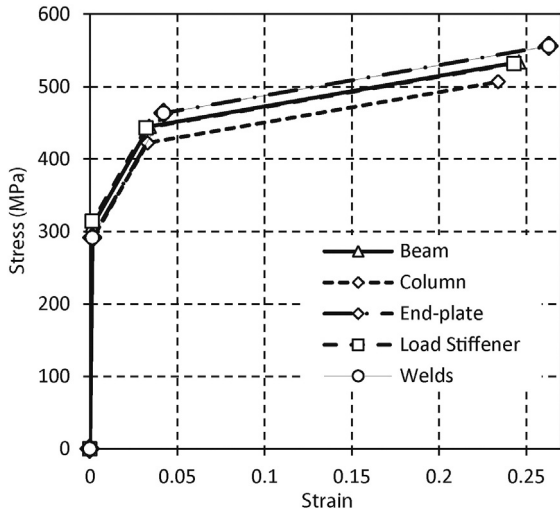
Fig. 5. Graphical representation of the materials' stress–strain tri-linear curve.

Fig. 7. Graphical representation of the three stage loading process [25].

(OMF), intermediate (IMF), or special (SMF) moment frames based on their ability to reach and sustain certain plastic rotational demands.

A connection may be classified as rigid, nominally pinned or semi-rigid according to Eurocode 3: Part 1-8 based on its boundary conditions. Fully welded connections, such as the so-called pre-Northridge connections, are considered fixed connections able to transfer both shear force and moment. They may be assumed to have a sufficient rotational stiffness to justify analysis based on full continuity. A nominally pinned connection should be able to transmit the internal forces without developing significant moments as well as capable of accepting the resulting rotations under the design loads. Semi-rigid connections provide a degree of interaction between members and should be capable of transmitting the internal forces and moments [1].

Welding tends to be expensive and is often done on site (usually avoided in the UK although it is quite common in some parts of the world) while bad climate conditions or poor workmanship can lead to low-quality welds altering the structural performance of the connection. Micro-cracks can lead to brittle failure when subjected to cyclic loads. Oppositely, bolted connections are considered more economical and provide faster assembly on site when compared to welded connections. An end-plate which is bolted to the column and welded to the beam can be an example of a partially restrained connection. End-plates are rising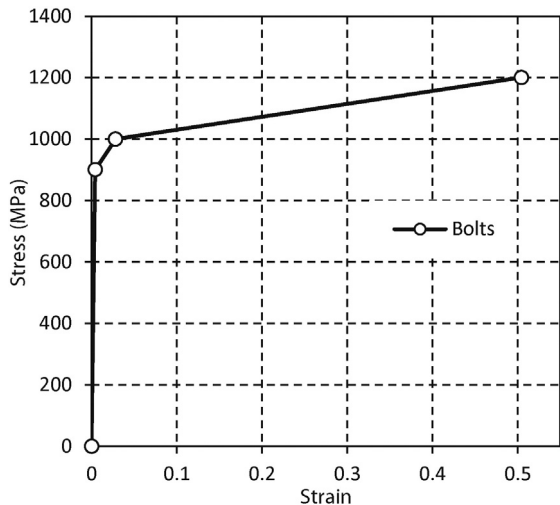 in popularity in steel MRFs due to their good structural behaviour (i.e. economy and ease of fabrication). The most studied bolted connections are the extended and double end-plate ones since the header and flush connections exhibit less strength and stiffness.

4. Study model

In the current study, due to the popularity of extended end-plate connections in seismic and wind active zones, a full three-dimensional (3D) FE model was created on [21], similarly to the FE model by Díaz et al. [22]. The model was based on the experimental test conducted by Janss et al. [23], named T101.010 — an exterior connection. This specific connection model was chosen for this study since it can be considered as a typical case of a bolted partially restrained beam-to-column end-plate connection. The FE model is first validated against the FE model by Díaz et al. [22], before conducting further parametric studies. Similarly to Maggi et al. [24], SOLID45, CONTA173 and TARGE170 were used in ANSYS v.14.0 software.

5. Validation of finite element model

5.1. FE model

The numerical results obtained from the FE analysis were compared with the experimental results by Janss et al. [23], the FE results from Díaz et al. [22], as well as with the results obtained using Eurocode 3, as shown later in Fig. 10. The dimensions and the detailed configuration of the modelled connection are summarised in Table 1 and Fig. 3.

Material nonlinearities were represented using a tri-linear stress–strain curve. The mechanical properties used for the connection are summarised in Table 2.

The tri-linear stress–strain used for the material behaviour is represented in Fig. 4. The elastic Moduli is as follows in the elastic region:

– Region (a): Young's modulus, E = 210,000 MPa and Poisson's ration, v, equal to 0.3.

The following two segments in the inelastic region represent the strain-hardening behaviour with reduced stiffness where:

– Region (b): $E_{h1} = {}^{E}/_{C_{WH}}$, with C_{WH} (work hardening coefficient) found to be equal to 50 from Díaz et al. [22].
– Region (c): $E_{h2} = {}^{E_{h1}}/_{10}$ so as to prevent convergence problems during the analysis.

Strains ε, ε_{h1} and ε_{h2} were derived for each material using their yield and ultimate strengths and the corresponding Moduli of each region.

Fig. 6. Graphical representation of the bolt's stress–strain tri-linear curve (M20 Class 10.9).

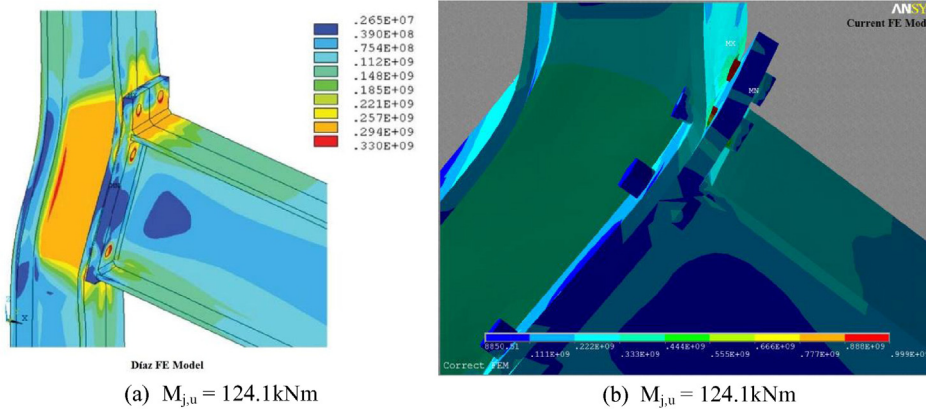**Fig. 8.** (a) Von-Mises stresses derived by [22], (b) elongation of bolts and opening between column flange and end-plate from the current study.

The stress–strain curves for all six materials were plotted and summarised in Figs. 5 and 6.

The 8-node solid elements (SOLID185) were used to mesh most solid elements including the beam, column, end-plate, bolts, welds and load stiffener. The bolts were modelled with 3D solid elements too; the shank was modelled by a 20 mm diameter cylinder, while the nut and head by hexagonally shaped solids. Right angle isosceles triangles were used to model the fillet welds using the weld throat thickness dimension.

Multiple contact regions were identified as follows:

– Contact between the bolt head and the end-plate
– Contact between the bolt nut and the end-plate
– Contact between the end-plate and the flange of the column
– Contact between the bolt shank and the openings of the end-plate/flange of column
– Contact between the beam and the end-plate (assumed 'initially bonded')
– Contact between the welds and the end-plate (assumed 'always bonded').

All six interfaces were modelled using contact elements CONTA174 and TARGE170. CONTA174 is used to represent contact and sliding between 3D target surfaces (TARGE170) as well as a deformable surface.
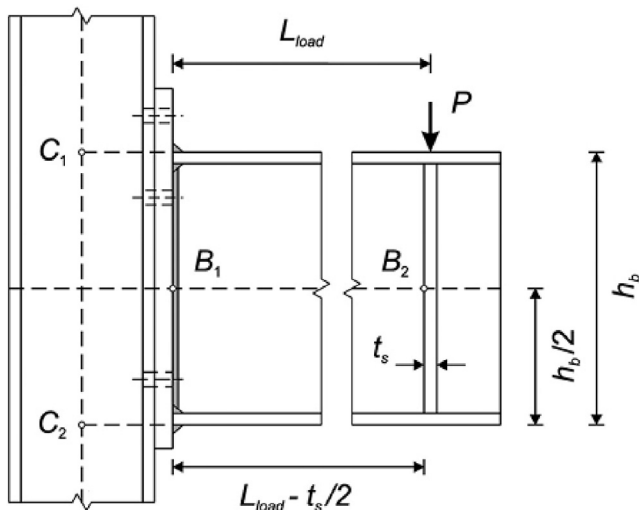
Contact occurs when the element surface penetrates one of the target segment elements.

5.2. Loading and analysis

In order to resemble the action of the loading apparatus during the experimental test, the load P was applied as a pressure (Pa) on the area represented by the projection of the load stiffener onto the top of the beam flange. The load was applied in three stages:

– Initially, load P was applied incrementally at a distance L_{load} (m) from the face of the column until the value of $M_{j,Rd,EC3}$ was reached, as the starting point of the plastic behaviour is unknown. This value $M_{j,Rd,EC3}$ corresponds to the design moment resistance of the connection at Eurocode 3 on the basis of the resistance of its basic components.

$$P_1 = \frac{M_{j,Rd,EC3}}{L_{load}} \tag{1}$$

$$P_1 = \frac{91.0581}{1.25} = 72.85 \text{ kN or}$$

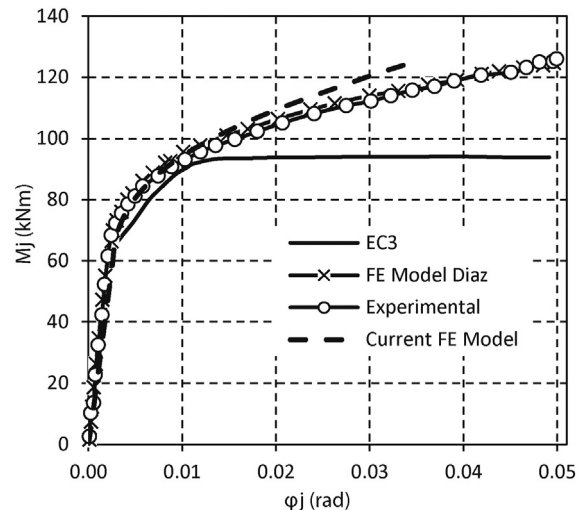$$P_1 = \frac{M_{j,Rd,EC3}}{L_{load}} \div (t_s) \times (b_{fb})$$

Fig. 9. Location of nodes B_1, B_2, C_1, and C_2 used for the moment-rotation curve [22].

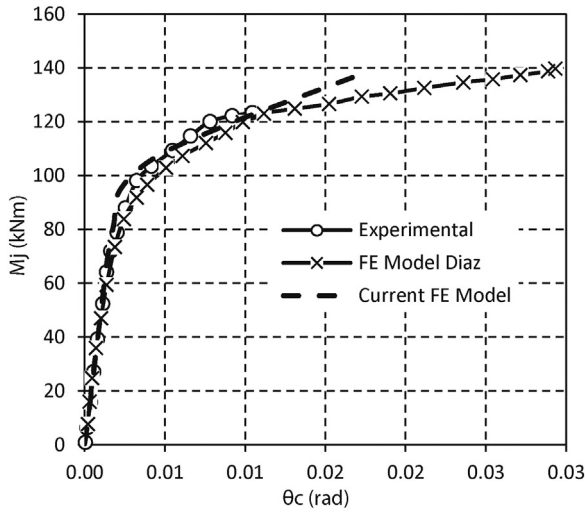**Fig. 10.** Comparison of moment–rotation (M_j–φ_j) curves.

Fig. 11. Comparison of moment–connection rotational deformation (M_j–θ_c) curves.

$$P_1 = \frac{91.0581}{1.25} \div (0.0108) \times (0.1509) = 44.7 \times 10^3 \text{ kN/m}^2.$$

– The model is then unloaded (i.e. $P_2 = 0$).
– Following, the load P is re-applied incrementally until the numerical solution fails to converge or, in order to decrease the computational costs, up to $^3/_2 \times M_{j,Rd,EC3}$.

$$P_3 = \frac{3 \times M_{j,Rd,EC3}}{2 \times L_{load}} \tag{2}$$

$$P_3 = \frac{3 \times 91.0581}{2 \times 1.25} = 109.27 \text{ kN or}$$

$$P_3 = \frac{3 \times M_{j,Rd,EC3}}{2 \times L_{load}} \div (t_s) \times (b_{fb})$$

$$P_3 = \frac{3 \times 91.0581}{2 \times 1.25} \div (0.0108) \times (0.1509) = 67.05 \times 10^3 \text{ kN/m}^2.$$

The nonlinear static analysis was performed using the full Newton–Raphson iteration scheme with the three load-steps described above. The three stage loading process of the loading (curve A–B), unloading (curve B–C) and reloading (curve A–D) is graphically represented in Fig. 7 below from [25]. $S_{j,ini,FEM}$ is the initial rotational stiffness.

A number of simplifications were made while designing the connection; the root radii of the beam and column and the washers of the bolts are not modelled in order to reduce the number of contact surfaces, bolt
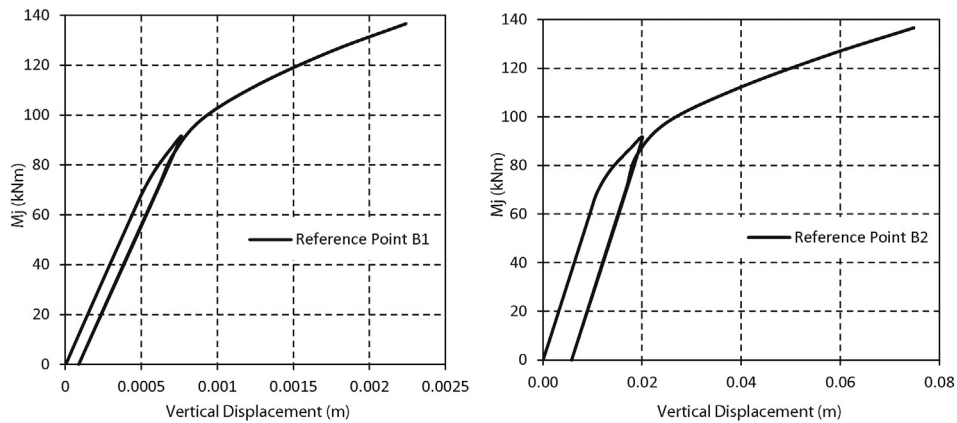
(a): Graphical representation of moment versus vertical displacement of point B_1 and B_2
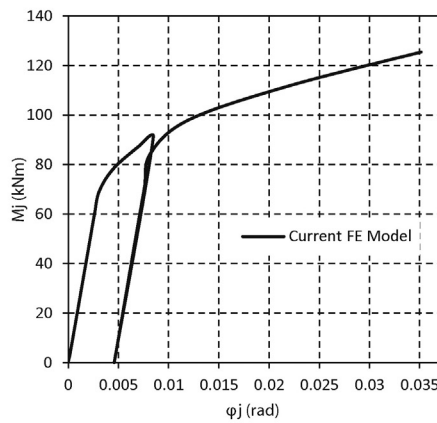
(b): Three-stage loading moment-rotation curve of current FE model

Fig. 12. (a): Graphical representation of moment against vertical displacement of point B_1 and B_2. (b): Three-stage loading moment–rotation curve of current FE model.

Table 3
Summarising table of FE parametric studies.

Model	Number of holes	Column face distance, S	Web opening spacing, S_o	Second web opening distance	Material properties	Column stiffeners	Flanges restrained
Solid	N/A	N/A	N/A	N/A	As experimental study	N/A	N/A
1	1 hole	200	1.2	N/A	As experimental study	N/A	N/A
2	2 holes	200	1.2	1.2	As experimental study	N/A	N/A
3	fully perforated	200	1.2	1.2	As experimental study	N/A	N/A
4	fully perforated	200	1.2	1.2	All S355 and Class 10.9 bolts	N/A	N/A
5	fully perforated	200	1.2	1.2	All S355 and Class 10.9 bolts	Yes	N/A
6	fully perforated	520	1.2	1.2	All S355 and Class 10.9 bolts	Yes	N/A
7	fully perforated	350	1.6	1.2	As experimental study	N/A	N/A
8	fully perforated	350	1.6	1.2	All S355 and Class 10.9 bolts	Yes	N/A
9	fully perforated	200	1.2	1.2	All S355 and Class 10.9 bolts	Yes	Yes
10	fully perforated	350	1.2	1.2	All S355 and Class 10.9 bolts	Yes	Yes
11	fully perforated	520	1.2	1.2	All S355 and Class 10.9 bolts	Yes	Yes

preloading is not included and the boundary conditions are applied directly to the column instead of the plates used in the particular experimental work.

5.3. Results of FE model

The results derived from the FE analysis were compared against the ones from the literature. The contour plots showed a satisfactory agreement with the FE results. The von-Mises plastic stresses for both loading levels ($M_j = 92.8$ kNm and $M_{j,u} = 124.1$ kNm) were compared.

The values of the von-Mises plastic strains of both FE models were very similar ranging from 0 to 0.011. Both models demonstrated a similar high plastic strain concentration in the column's shear panel zone of about 0.005 to 0.006. Additionally, a similar von-Mises stress distribution was achieved, around 300 MPa in the shear panel zone.

The openings between the end-plate and the column flange as well as the elongation of the bolts (with high stresses along the bolt shanks) were demonstrated by the FE model, as it can be seen in Fig. 8b.

To evaluate the behaviour of a beam-to-column connection, the bending moment applied to the connection, M_j, was plotted against the corresponding rotational deformation, φ_j. In addition, the bending moment applied, M_j, was also plotted against the connection's rotational deformation, θ_c.

The bending moment of the connection is found by multiplying the applied load, P (kN), by the distance L_{load} (m), which corresponds to the distance between the application point of the load and the face of the end-plate. Displacement values for specific nodes (B_1, B_2, C_1, and C_2)

extracted from [21] were used to calculate the rotational deformation, φ_j, the shear deformation of the column weak panel zone, γ, and the connection's rotational deformation, θ_c. The relationship between all three terms, according to Bursi and Jaspart [26], can be given as: $\varphi_j = \theta_c + \gamma$. The location of the nodes used to calculate the rotational deformation is shown in Fig. 9.

The following equations were used to calculate the parameters:

$$\varphi_j = atan\left(\frac{V_{B2} - V_{B1}}{d_b}\right) - \theta_{el,c} - \theta_{el,b} \text{ (radians)} \tag{3}$$

with V_{B1} and V_{B2} are the vertical displacements (y-axis) of nodes B_1 and B_2; d_b is the distance between those two nodes which corresponds to $d_b = L_{load} - \frac{t_s}{2} = 1.25 - \frac{0.0108}{2} = 1.2446$ m.

$\theta_{el,c}$ and $\theta_{el,b}$ were derived from Girão Coelho and Bijlaard [27] experimental study and represent the theoretical column and beam elastic rotations.

$$\theta_{el,c} = \frac{5}{64} \times \frac{M_j(H - h_c)}{E \times I_c} \text{ (radians)} \tag{4}$$

$$\theta_{el,b} = -\frac{P_{load}}{E \times I_c} \times \left[\frac{d_b^2}{6} - \frac{L_{load} \times d_b}{2}\right] \text{ (radians)} \tag{5}$$

where E is the Young's modulus, $E = 210$ kN/mm²; P_{load} is the applied load (kN), M_j is the moment of the connection (kNm); the column
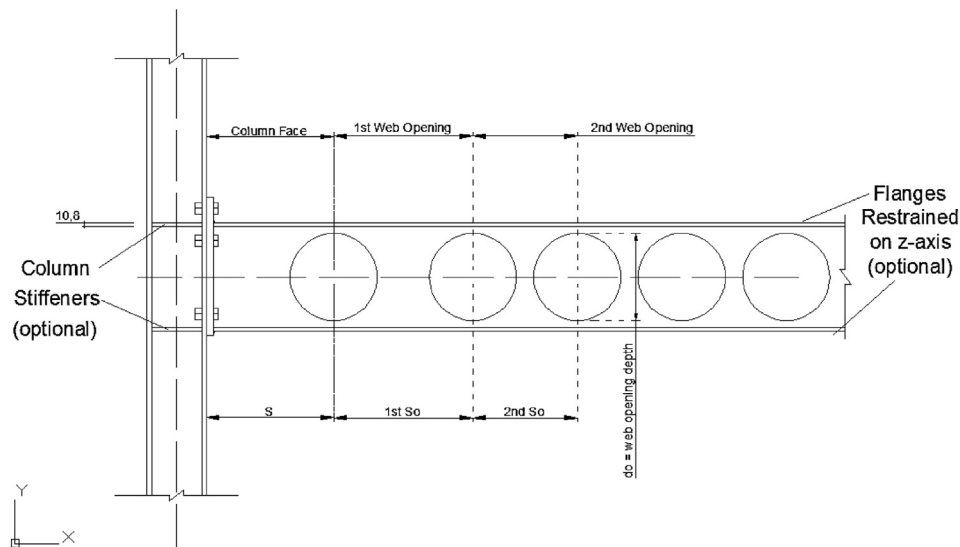

Fig. 13. Semi-rigid beam-to-column connection showing geometrical parameters.

length H = 3.625 m and the column's height h_c = 0.1625 m; I_c and I_b are the second moment of areas of the column and beam, respectively.

By geometry and by ignoring the root radius while it is not included in the FE model:

$$I_c = \frac{1}{12}\left[b_{fc} \times h_c{}^3 - (b_{fc} - t_{wc}) \times (h_c - 2 \times t_{fc})^3\right] \tag{6}$$

$$I_c = \frac{1}{12}\left[0.1601 \times 0.1625^3 - (0.1601 - 0.0085) \times (0.1625 - 2 \times 0.0126)^3\right]$$

$I_c = 24,550,700$ mm^4 for the column

$$I_b = \frac{1}{12}\left[b_{fb} \times h_b{}^3 - (b_{fb} - t_{wb}) \times (h_b - 2 \times t_{fb})^3\right] \tag{7}$$

$$I_b = \frac{1}{12}\left[0.1509 \times 0.2989^3 - (0.1509 - 0.0073) \times (0.2989 - 2 \times 0.0108)^3\right]$$

$I_b = 80,637,900$ mm^4 for the beam.

The shear deformation of the column weak panel zone, γ, is found by:

$$\gamma = \operatorname{atan}\left(\frac{U_{C2} - U_{C1}}{h_b}\right) - \theta_{el,c} \text{ (radians)} \tag{8}$$

where U_{C1} and U_{C2} are the horizontal displacements (x-axis) of the nodes C_1 and C_2, and h_b is the distance between those two nodes which corresponds to the height of the beam h_b = 0.2989 m.

Plotting the ($M_j - \varphi_j$) and ($M_j - \theta_c$) graphs and comparing with the results produced by the previous FE model of the same connection, a satisfactory correlation was achieved and hence, the elaborated model can be further used for the parametric investigation (Figs. 10 and 11).

Fig. 12 demonstrates the moment against the vertical displacements at reference points B_1 and B_2 showing all three aforementioned loading-unloading stages.

By referring to this graph, it is noticed that the angle of the unloading line (i.e. $S_{j,ini,FEM}$: initial rotational stiffness) corresponds to that of the first loading (curve A–B) which shows an adequate moment and rotational capacity of the connection.

6. Parametric studies

6.1. Introduction

A semi-rigid steel beam-to-column connection with circular web openings was examined in the parametric study and subjected to cyclic loading. The web-post buckling behaviour was investigated for multiple
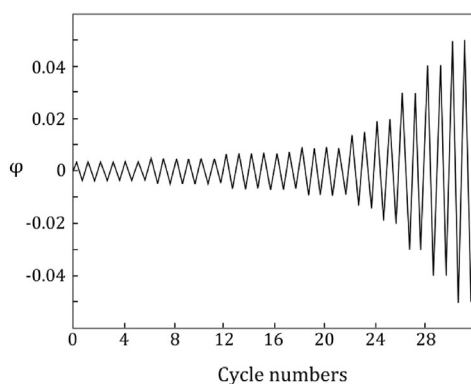
Table 4
Beam end displacements for cyclic loading sequence.

Number of cycles	Peak deformation φ (radians)	Load-steps (accumulative)	End displacements Δ_{LC} (m)
6	0.00375	12	0.0116297
6	0.005	24	0.0155063
6	0.0075	36	0.0232594
4	0.01	44	0.0310125
2	0.015	48	0.0465188
2	0.02	52	0.0620250
2	0.03	56	0.0930375
2	0.04	60	0.1240500
2	0.05	64	0.1550625

both closely as well as widely spaced web openings along the length of the beam.

In order to fully understand the response of RWS connections with cellular beams and evaluate their ability to dissipate seismic energy, numerous models including a Solid beam Model without web openings were employed. A total of 11 FE models were developed and categorised into four Sets, as summarised in Table 3.

The same connection configuration as in the validation study is used herein, whilst the length from the end-plate to the load application point, L_{load}, is different. The beam length was increased in order to be able to accommodate multiple web openings and simulate a beam length of 6 m. Consequently, the load application was extended from 1.25 m in the validation study, to 3 m in all four parametric studies.

The hysteretic behaviours and stress distribution plots were scrutinised in all cases to ease comparison and establish meaningful results despite the number of geometric parameters assessed.

6.2. Parameters

The geometrical parameters examined and referred in Table 3, can be seen in Fig. 13 and are as follows:

- The web opening diameter, d_o;
- The distance from the face of the column to the centreline of the first web opening, S;
- The distance between adjacent web openings taken from their respective centrelines, S_o.

In some models the beam flanges were restrained transverse to the web and/or include column stiffeners (Fig. 13) in order to avoid lateral torsional buckling (LTB) of the perforated beam as well as high stresses concentration in the shear panel zone. In engineering practice, column stiffeners are necessary, and continuous lateral restraint is provided to
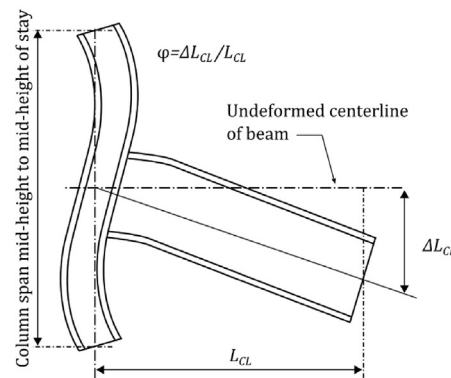

Fig. 14. SAC cycling loading sequence (left), angular rotation of assembly (right); FEMA-350.
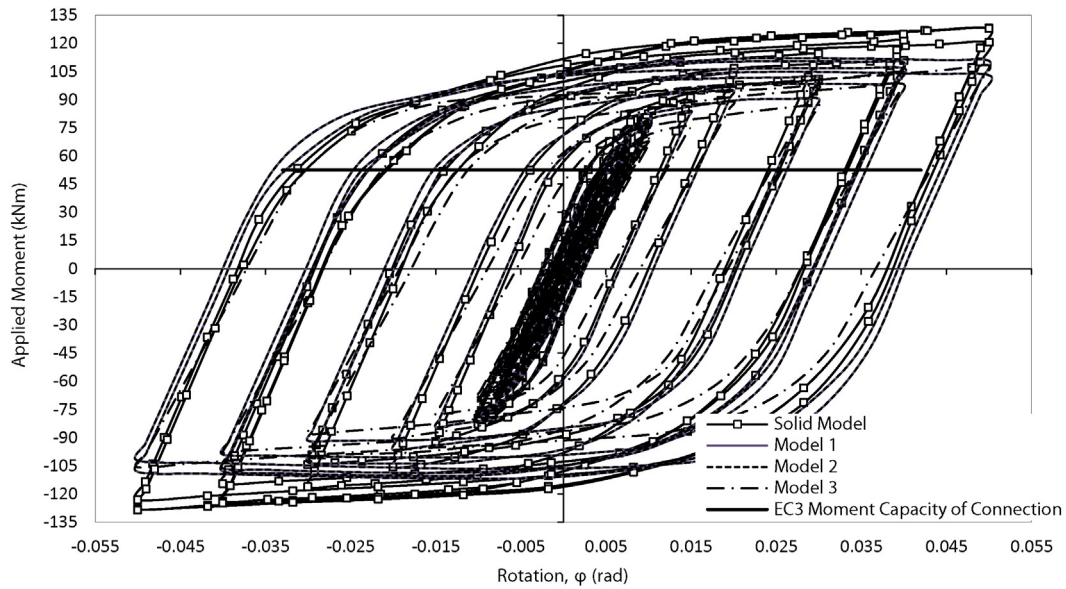
Fig. 15. Moment–rotation curves of Solid beam Model and Models 1, 2 and 3.

the beams by the concrete slab. Slabs are not modelled on an effort to record the worst case loading scenario. However, the emphasis of the current study is on the geometric parameters of the cellular beams instead, hence restraints only used to ease the computational analysis and support the conduction of the full cyclic loading.

For all parametric analyses, the web opening depth, d_o, was taken as equal to $0.8h_b$, where h_b is the height of the beam, hence:

$$d_o = 0.8 \times h_b = 0.8 \times 0.2989 = 0.23912 \text{ m}.$$

This extreme opening depth was introduced by Tsavdaridis and D'Mello [16,17] in order to promote lighter perforated beams as well as deeper sections which provide large web opening areas (WOA) for the integration of services without compromising the capacity of

the beams in the most severe failure modes. The previous widely-accepted limit for the d_o was equal to 0.75h [28]. The use of such large web openings in the design of RWS connected has proven adequate performance in certain cases investigated so far while it can have an impact on the connection's strength [18].

Three values of the distance, S, were examined (200 mm, 350 mm and 520 mm). Tsavdaridis et al. [13] suggested that parameter S proved to be dependent on the opening's geometry and WOA. The value of 200 mm was taken to account for the least favourable scenario in design practice, having a large WOA and a small distance from the face of the end-plate which would maximise the stress concentrations near the face of the column.

Tsavdaridis and D'Mello [14,15] also investigated the effect of eight S_o/d_o ratios ranging from 1.1 to 1.8. For closely spaced web openings,
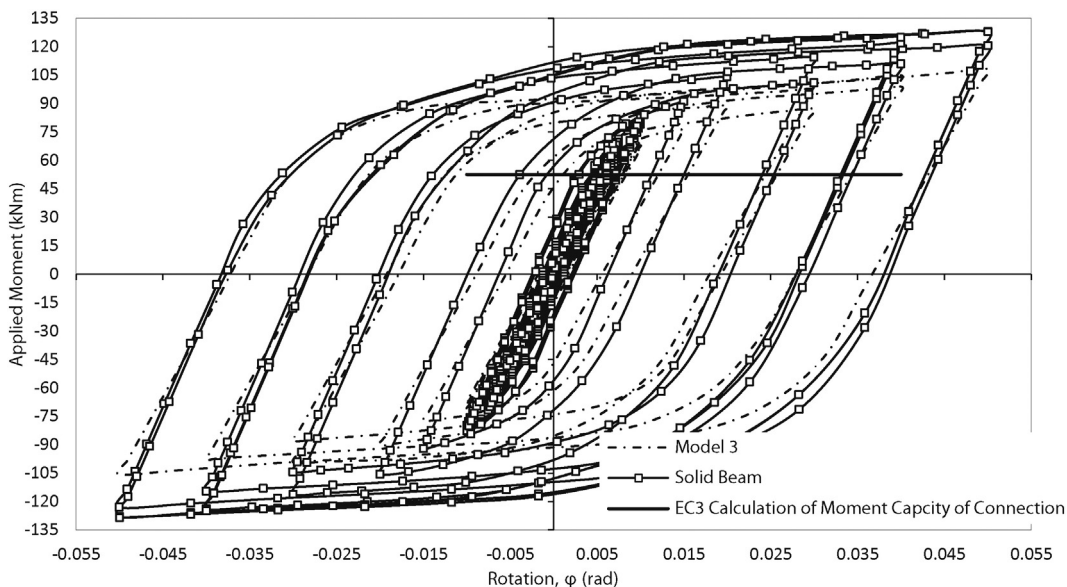

Fig. 16. Moment–rotation curves of Solid and fully-perforated beams.

the optimum ratios were found to be from 1.1 to 1.3 and showed adequate web-post behaviour when novel elliptically-based web openings were further utilised.

The distance between adjacent circular web openings, S_o, for closely spaced openings is therefore taken for the current study as equal to $1.2d_o$, while for largely spaced openings, $S_o = 1.6d_o$.

$$S_o = 1.2 \times d_o = 1.2 \times 0.8 \times h_b = 1.2 \times 0.23912$$
$$= 0.286944 \text{ m (closely spaced)}$$

$$S_o = 1.6 \times d_o = 1.6 \times 0.8 \times h_b = 1.6 \times 0.23912$$
$$= 0.382592 \text{ m (largely spaced)}$$

6.3. Loading sequence and analysis

The specimen was loaded cyclically following the SAC loading protocol recommended by [3], in order to identify its main seismic response characteristics. Beam end displacements were applied at the location of the beam's stiffener, with an upward and a downward displacement producing one cycle of the loading protocol. A total of 32 cycles, equivalent to 64 applied displacements, were computed. Each load-step is applied in 100 sub-steps which could automatically be varied by [21] to achieve convergence on a range from 10 to 1000 sub-steps due to the geometric and material nonlinearities. The SAC loading protocol is shown in Fig. 14 and Table 4 summarises the displacements values, Δ_{LC}, applied as load-steps.

Distance L_{LC} from the centreline of the column to the centreline of the load stiffener is equal to:

$$L_{LC} = L_{Load} + t_{ep} + \frac{h_c}{2} = 3 + 0.02 + \frac{0.1625}{2} = 3.10125 \text{ m}.$$

An Eigen buckling analysis was initially reformed to derive the first Eigen mode shape, hence small imperfections, which were then used after being scaled by the recommended factor by [14] of $t_w/200 = 7.3/200 = 0.0365$ mm to update the geometry. Following, a nonlinear (geometric and material) analysis was performed with the full 64 load-steps using the "Newton–Raphson" approach.

6.4. Results: Solid beam Model & Set 1 (Models 1, 2 and 3)

6.4.1. Hysteretic behaviour

The moment–rotation (M–θ) curves were derived from each analysis to present the hysteretic performance of the beam-to-column connections and particular characteristics including the initial rotational stiffness, rotational capacity, strength (ultimate moment capacity) and the amount of energy dissipated. Such hysteretic curves were established from information derived by [21]; vertical y-axis nodal

displacements were recorded at the column centreline and at the end of the beam where the stiffener is located, as well as nodal reactions corresponding to the applied displacement for each load-step. The rotations were determined from:

$$\varphi = \frac{\text{Stiffener End Displacement} - \text{Column Centreline Diplacement}}{\text{Distance from Column Centreline to Stiffener Location}}.$$

The moment capacity was taken at the column centreline and corresponds to:

$$M = |\text{Reaction}|$$
$$\times \text{Distance from Column Centreline to Stiffener Location}.$$

The four hysteretic curves were superposed and are shown in Fig. 15.

Comparing these four graphs Fig. 15, it is noticed that the Solid beam Model (of the same depth) without web openings achieved the highest moment capacity of approximately 125 kNm. Therefore, there is a decrease in moment capacity for the case of Model 1 and Model 2 (110 kNm and 115 kNm, respectively), whereas the lower moment capacity is achieved for the case of the fully perforated beam (Model 3 with 10 openings) with 105 kNm (Fig. 16). This slight decrease is ideal to ensure that the connection between the beam and the column is stronger than the connected beam such that the plasticity is developed in the ductile beam section rather than the connection which has very limited ductility (i.e. the connections are over-strengthed and force plastic hinges into the beam). Deep perforated beams in comparison with the initial parent Solid sections, often provide high moment capacity; however the optimum location of the first web opening as well as the spacing and the shape of the rest openings ensure the balanced design. Intentionally, a deep beam with a shallow column design was chosen for this study, with scope to achieve increased ductility and mobilisation of stresses from the column and the connection towards the beam although an extreme and unlike scenario in seismic-resistant design of steel structures.

Further observations were made regarding the ultimate rotational capacity of each specimen. By referring to the above graphs, all specimens achieved an ultimate rotational capacity of about 0.05 rad making RWS suitable for SMF or IMF systems in seismically active zones . The introduction of web openings has reduced the total moment capacity without reducing the ultimate rotational capacity. Model 3 with the cellular beam shows an increased ductility of the connection and lower strength degradation towards the final cycles when compared to the Solid beam Model and Model 1. All models generally showed a gradual strength degradation which is in accordance with Tsavdaridis et al. [13] observations, and this is typical for beams with deep web openings (0.8h). Models 1 and 2 showed an additional amount of strength reduction due to local web buckling at certain cycles. Table 5 summarises the

Table 5
Results summary table for Set 1.

Specimen	Number of circular openings	Yield moment M_y (kNm)	Ultimate moment M_u (kNm)	Yield rotation φ_y (rad)	Ultimate rotation φ_u (rad)
Solid beam	–	74.59	128.58	0.009595	0.049989
Model 1	1	71.14	112.19	0.009492	0.050025
Model 2	2	64.41	117.23	0.009292	0.050025
Model 3	10	62.44	105.77	0.008555	0.05004

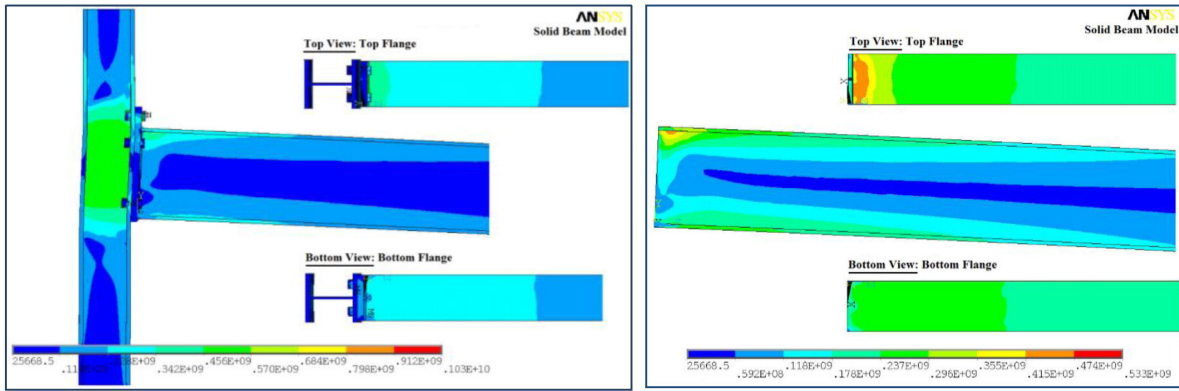| Specimen	Rotational ductility D_φ	Initial rotational stiffness K_i (kNm/rad)	Web opening area (mm^2)	Dissipated energy E (kNm) (rad)
Solid beam	5.21	10,540.12	–	145.90
Model 1	5.27	10,394.84	44,907.8	124.26
Model 2	5.38	9542.74	44,907.8	114.52
Model 3	5.85	8226.04	44,907.8	72.11

Fig. 17. Von-Mises stress contour plots of Solid beam Model (loading at 155.1 mm, cycle 32).

results derived from the hysteretic curves. The initial rotational stiffness is calculated from the first cycle of the analysis and corresponds to:

Initial Rotational Stiffness, $K_i = \dfrac{M}{\varphi}$.

The rotational ductility was found to be equal to:

Rotational Ductility, $D_\varphi = \dfrac{\varphi_u}{\varphi_y}$.

The WOA corresponds to the area of the opening:

$$WOA = \pi \times \left(\frac{d_o}{2}\right)^2 = \pi \times \left(\frac{239.12}{2}\right)^2 = 44907.8 \text{ mm}^2.$$

The energy dissipated, E, is equivalent to the area under the hysteretic curve which is computed using the trapezoidal rule where:

$$Area\ Increment = (\varphi_2 - \varphi_1) \times \left[\frac{M_1 + M_2}{2}\right].$$

Moreover, it was observed that the initial rotational stiffness decreased with the introduction of web openings. When the two extreme cases were plotted, the initial rotational stiffness was found steeper for the Solid beam Model. The rotational stiffness decreased by 1%, 11.3% and 21.6% for Model 1, Model 2 and Model 3, respectively.

The horizontal threshold line corresponds to the moment capacity of the connection (52.5 kNm) as calculated using Eurocode 3. Eurocode 3

connection capacities for moment resistance cannot distinguish between a beam with or without a web perforation as the beam web is unlikely to be a critical component unless the hole is directly next to the endplate (component 7 and 8 in Table 6.1 of EC3-1-8). Furthermore, Eurocode 3 resistances are "design values" and have a number of partial safety factors that limit the predicted capacity.

In detail, the introduction of multiple web openings (ten openings) reduces the moment capacity by 17.7% while the ultimate rotation was almost unchanged in all cases. Consequently, the dissipated energy is higher for the Solid beam case since higher moment capacities were reached, provided that the column and the connection are strong enough to withstand the forces acting from the beam without developing plastic hinges and hence developing the soft-storey mechanism. In order to fully understand the lack of dissipated energy in certain cases, the stress distribution was analysed.

6.4.2. Stress distribution

The von-Mises stresses for all four models were plotted (Figs. 17, 18, 19 and 21) to examine the behaviour of the connections. Stresses in the beams were also highlighted separately, to further visualise the stress distribution in the vicinity of the web openings. Ideally, in order to mobilise the stresses away from the column and the connection assembly, a Vierendeel mechanism should be formed. Local bending moments, known as Vierendeel moments lead to the creation of four plastic hinges above and below the web opening at particular angles.

Assessing the connection using the Solid beam Model (Fig. 17), it was noticed that the stress was concentrated in the shear panel zone of the column, reaching its ultimate strength of 422 MPa. The highest
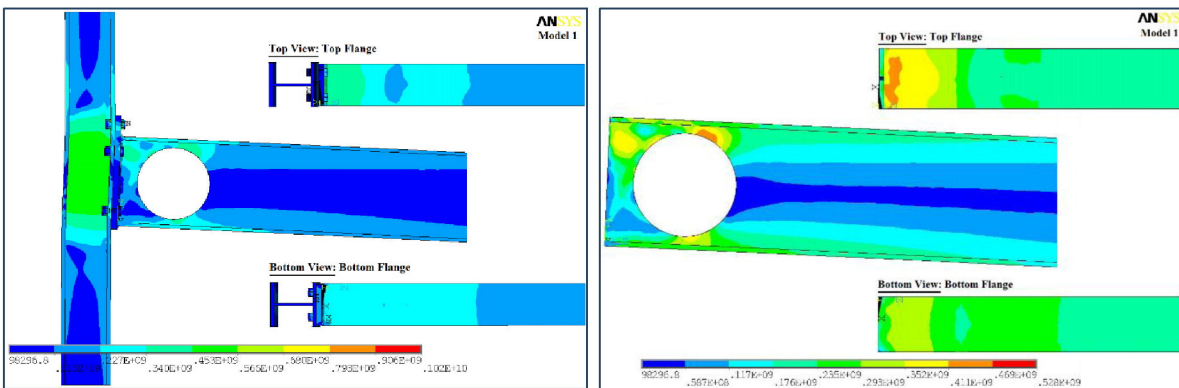

Fig. 18. Von-Mises stress contour plots of Model 1 (loading at 124.1 mm, cycle 31).
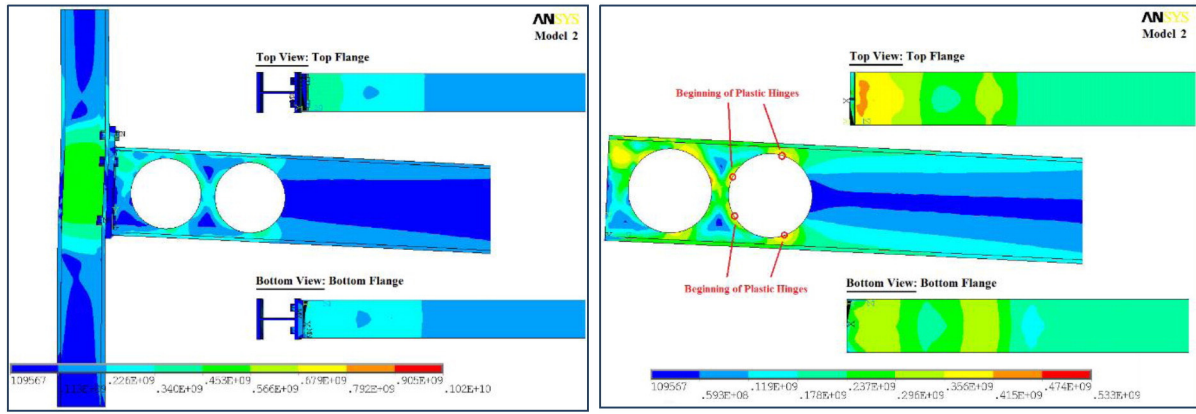
Fig. 19. Von-Mises stress contour plots of Model 2 (loading at 124.1 mm, cycle 31).
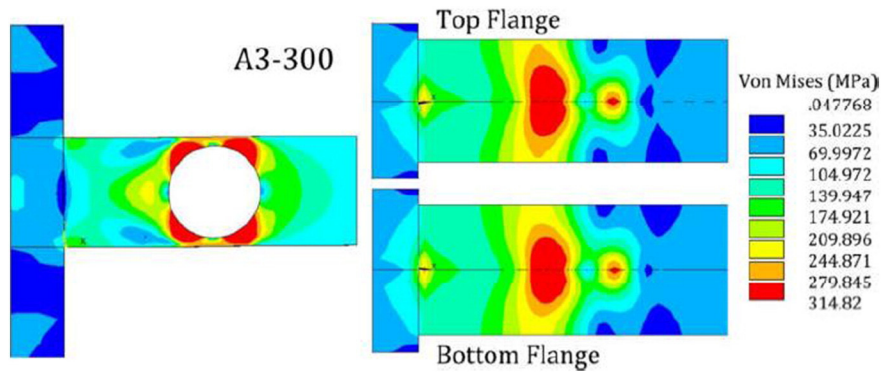

Fig. 20. Complete Vierendeel mechanism and formation of plastic hinges, loading at 8.6 mm [13].

stresses were observed in the top row bolts, due to high tension forces, at almost 1000 MPa. The stresses away from the column and in the beam have remained low, expanding to the flanges of the beam before reaching the beam web.

The introduction of web openings mobilised the stresses towards the beam. It was found that both models reduced the amount of stress in the panel zone, without, however, shifting the stresses entirely to the beam. The full plastic hinges were not formed as the stress (between 350 MPa and 400 MPa) had not reached the ultimate strength of the beam of 445 MPa. High stresses found in the column panel zone and in the top row bolts, hence the Vierendeel mechanism did not take place. An indicative representation of a complete Vierendeel mechanism for connections with a perforated beam is depicted in Fig. 20. It

was concluded that both the particular connection type and the size of the column in relation to the beam, as well as the chosen material properties play a significant role in the formation of the Vierendeel mechanism.

Comparing the current model with the one from the literature, it was realised that the development of the ideal plastic hinges obtained were associated with a beam using the same diameter of a web opening, but at a greater distance from the column face (S = 300 mm). Additionally, the connection was fully welded. In the current study having a distance of S = 200 mm and a bolted connection, the stresses were increased in the critical area close to the column face.

By introducing an additional second web opening in Model 2 (Fig. 19), more stresses were mobilised from the critical zone to the
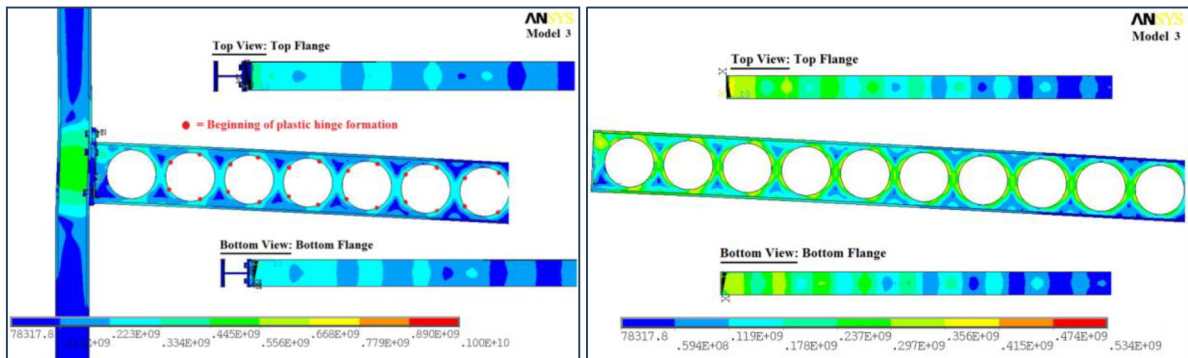

Fig. 21. Von-Mises stress contour plots of Model 3 (loading at 93.1 mm, cycle 28).
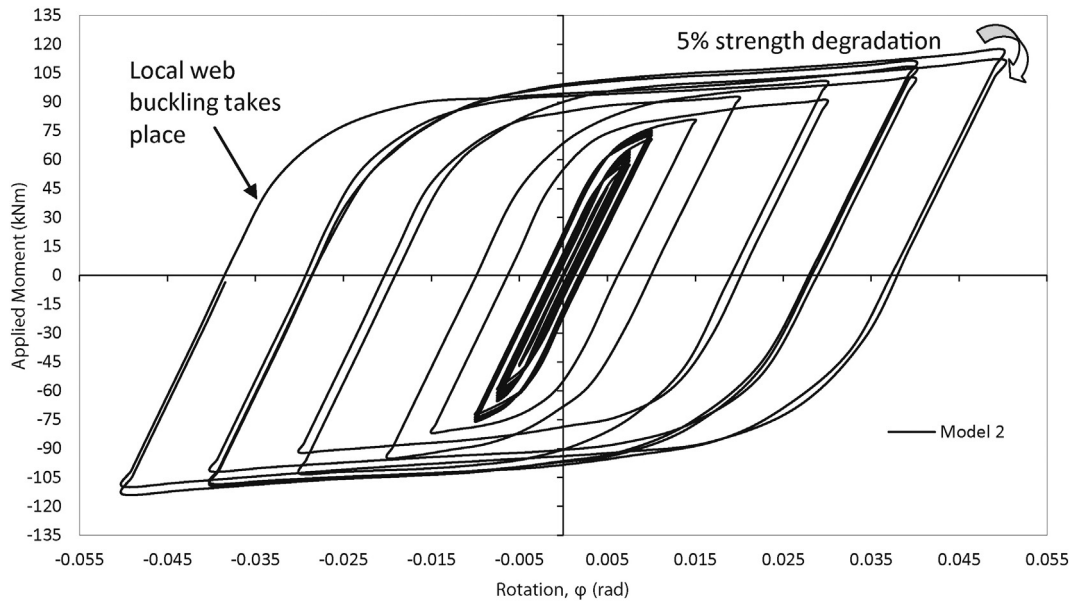
Fig. 22. Strength degradation after web local buckling of Model 2.

second web opening and a pattern of four plastic hinges began to appear at various angles. However, the stress magnitude in the panel zone of the column was still high. Stresses in the top and bottom flanges were moved further away from the column while the high-stress intensity in the top flange, due to the top row of bolts, was slightly decreased. The distance between the web openings being of $1.2d_o$ resulted in the high stress concentration of the web-post between the openings.

Eventually, the high stresses in the shear panel zone decreased gradually in Model 3 (Fig. 21) and the hinges mobilised further away from the connection. The final position of such hinges was the same for all circular openings, except for the first one which is located very close to the connection. The top and bottom views demonstrate that the highest stresses in the beam were found in the vicinity of the first two perforations as discussed in Model 2.

The out-of-plane displacements were also recorded at the mid-height of the first web-post. Similarly to the observation presented by Tsavdaridis et al. [13], the dominant failure mode for perforated beams with an opening diameter equal to 0.8h, was the Vierendeel mechanism, while the web buckling is more noticeable in smaller openings (such as when $d_o = 0.5h$) where the it is unlikely to obtain the Vierendeel mechanism. In Model 2, the initiation of web local buckling

was also related to some strength degradation (Fig. 22). During the last two cycles (31 and 32), where the out-of-plane displacement increased, the strength reduced slightly by about 5%.

6.4.3. Synopsis from initial findings and further considerations

All four models achieved an acceptable ultimate rotational capacity to be used in the seismic design.

While the introduction of perforations reduced the strength of the beam, it consequently affected the moment capacity of the connection as well as the initial rotational stiffness, while the ultimate rotational capacity and the rotational ductility were increased. The influence of geometric parameters was also examined by analysing the stress distribution. Large openings in the range of 0.8h were proved in previous studies to promote the creation of four plastic hinges and experience little to no local web buckling when located at certain positions. Hereby, the plastic hinges did not completely form, as stresses in web panel zone of the column and in the top row of bolts were dominant due to the connection configuration, section sizes and the particular end distance, S. The energy dissipation was slightly reduced in Model 1 and 2 and decreased by almost half in the case of the cellular beam (Model 3) in comparison to the Solid beam Model. To further promote the full understanding of the mechanisms developed in the current investigation of RWS connections, the following changes were assigned:

- The same nominal material strength to the member of the connection of S355 steel grade and M10 bolts;
- Increase the end distance, S, from the face of the column, so as to investigate the critical location of the first opening;
- Increase the web opening spacing for the first two perforations while experience high stresses (i.e. widely spaced first two web openings followed by a closely spaced typical cellular beam — such design also promotes the 'weak-link' concept used in the design of 'replaceable structural fuses' that absorb the seismic energy as the frame rocks and can be replaced following the event).

Consequently, additional FE models were developed to witness whether these modifications result in an enhanced structural performance of RWS connections subjected to cyclic loading. Since this study is focusing on the introduction of fully penetrated beams with a series of web openings in the design of MRFs, only typical cellular beams will be used for the remaining analyses.
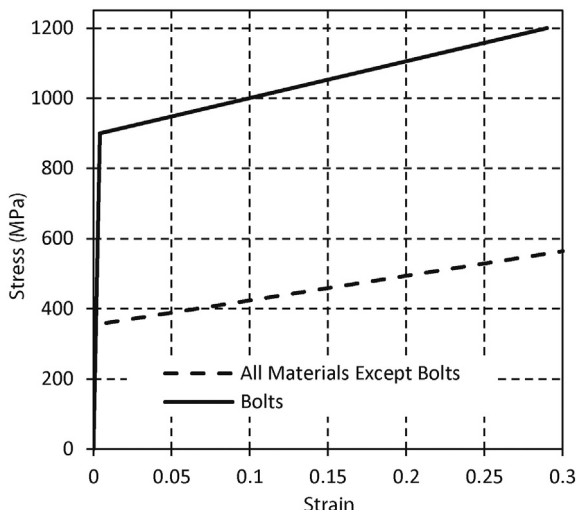

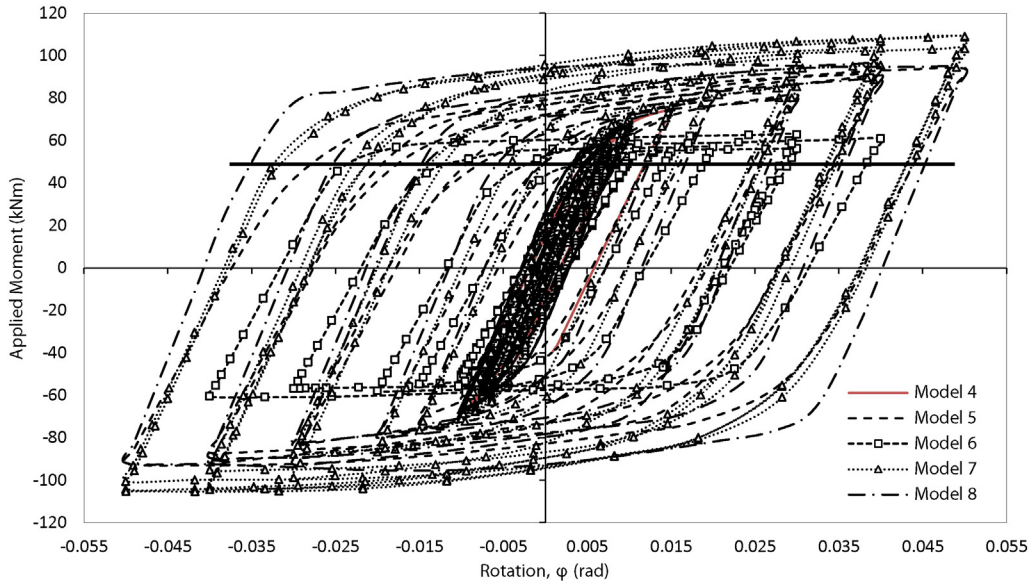**Fig. 23.** Graphical representation of the revised material's stress–strain bi-linear curves.
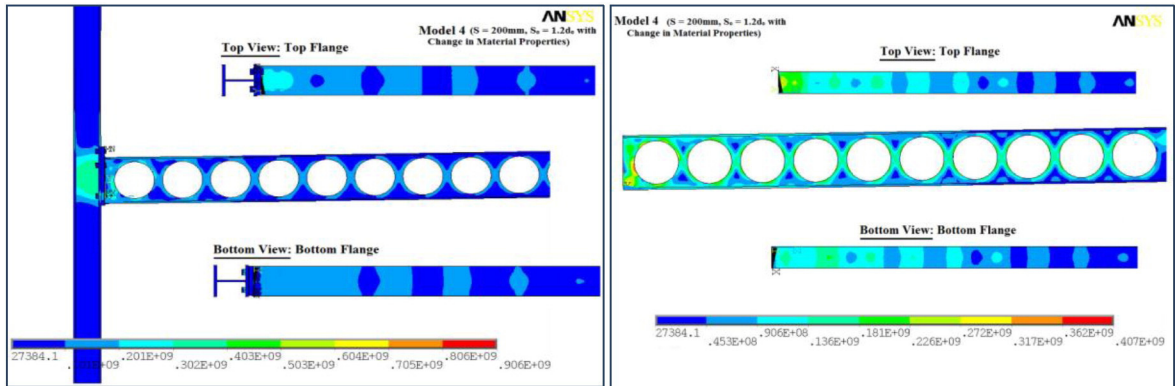
Fig. 24. Moment–rotation curves of FE Sets 2 and 3.

Fig. 25. Von-Mises stress contour plots of Model 4 (loading at 46.5 mm, cycle 23).
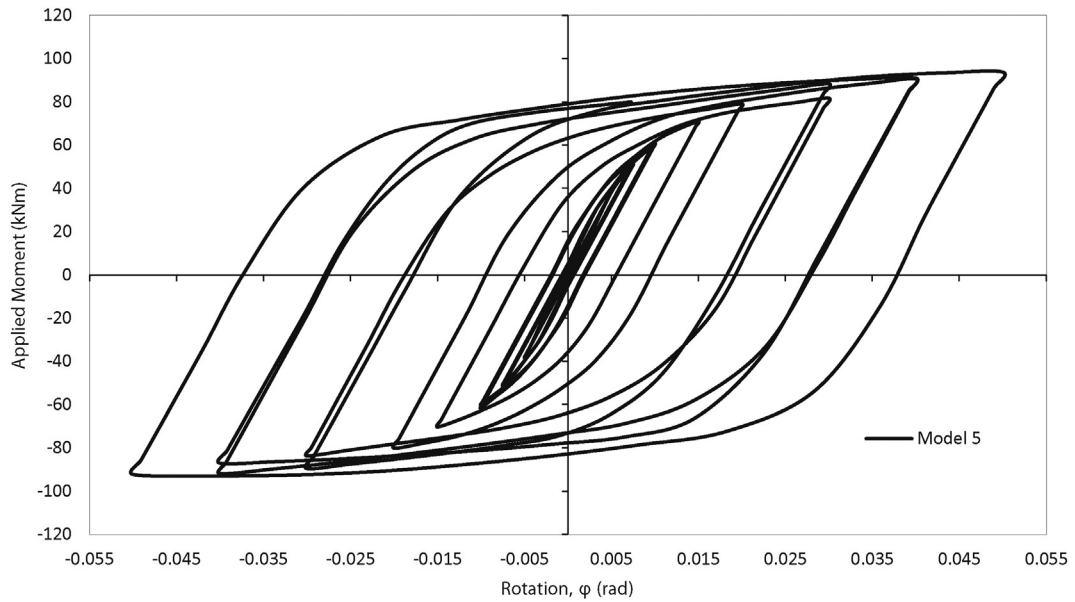

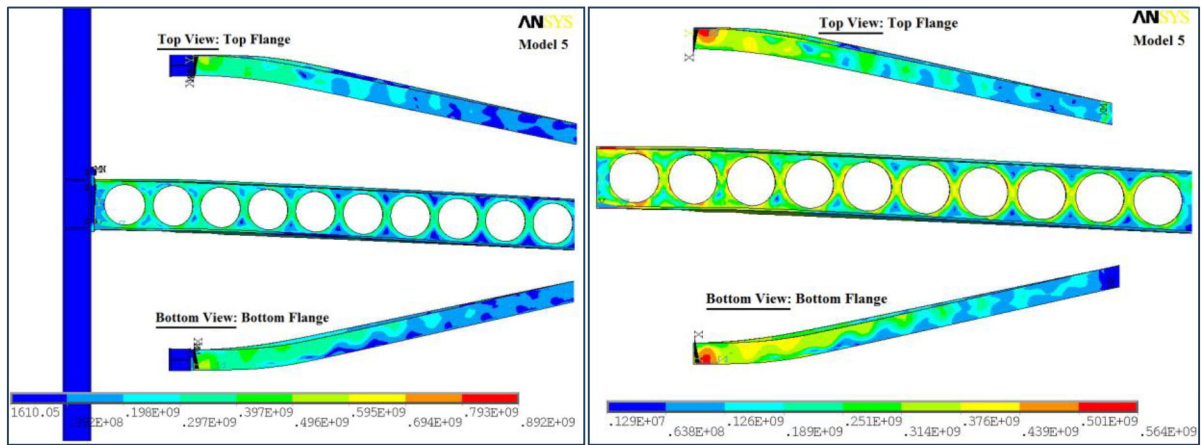**Fig. 26.** Moment–rotation curves of Model 5.

Fig. 27. Von-Mises stress contour plots of Model 5 (loading at 124.1 mm, cycle 29).

6.5. Results: Sets 2 and 3 (Models 4, 5, 6, 7 and 8)

Models 4, 5 and 6 contain closely spaced web openings while Models 7 and 8 contain the first web opening at a wider distance from the second one, and then followed by closely spaced ones.

In Set 1, the yield and ultimate strengths of the beam (308.5 MPa and 445 MPa) were somewhat higher than that of the column (289.4 MPa and 422.2 MPa) similar to the model used for the experimental and the validation study. The difference in the mechanical properties of the components (but also the section properties of the connected members) might hinder the "*weak beam-strong column*" mechanism. Hence, all materials were assumed to be of S355 steel grade with yield and ultimate strengths of 355 MPa and 470 MPa, respectively; except for the M10 bolts, where yield strength of 900 MPa and ultimate of 1000 MPa were used. This change in material properties is applied for Models 4, 5, 6 and 8. In addition, common bi-linear stress–strain curves were adopted with adjustments made on the work hardening coefficient, C_{WH}, of the Tangent Modulus, E_T. The previously used tri-linear stress–strain curves resulted in a somewhat strong connection with the bolts behaving in a very stiff manner, particularly due to the low work hardening coefficient value of 50 used for the middle linear stiffness. The bi-linear curves (Fig. 23) use a work hardening coefficient of 300 for all

components, except the bolts in which a value of 200 was used. These values result in Tangent Moduli of 700 MPa and 1050 MPa for all components and bolts, respectively, and are in agreement with the Eurocode 3 suggestion:

$$E_T = \frac{E}{C_{WH}}.$$

6.5.1. Model 4

The hysteretic curves of Sets 2 and 3 are plotted in Fig. 24. To effectively assess the impact of the changes in material properties on the hysteretic behaviour of the connection, the same geometric parameter configurations as for Model 3 were used. The full 64 load-step analysis failed to converge at load-step 46. The hysteretic curve showed a low maximum ultimate rotation of only 0.015 rad and an ultimate moment of 74.27 kNm which are significantly lower than those of 0.05 rad and 105.77 kNm achieved before making the changes in the material properties.

Plotting the von-Mises stress plots and from Fig. 25, it is apparent that some stress was still present in the shear panel zone of the column and in the same range of the stress the web beam experiences close to
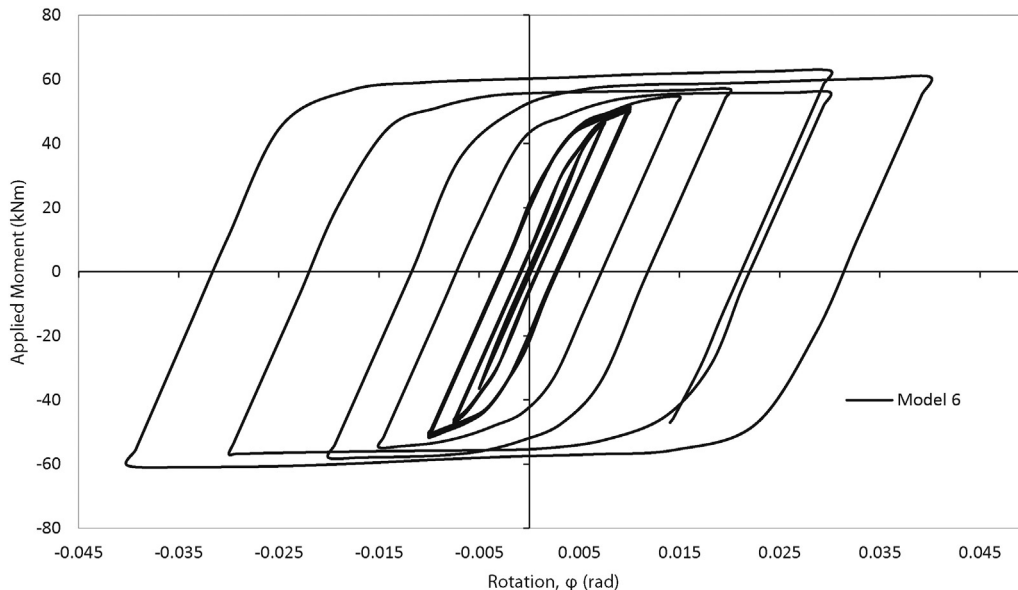

Fig. 28. Hysteretic curve of Model 6 (S = 520 mm, S_o = 1.2d_o, with change in material properties and column stiffener).
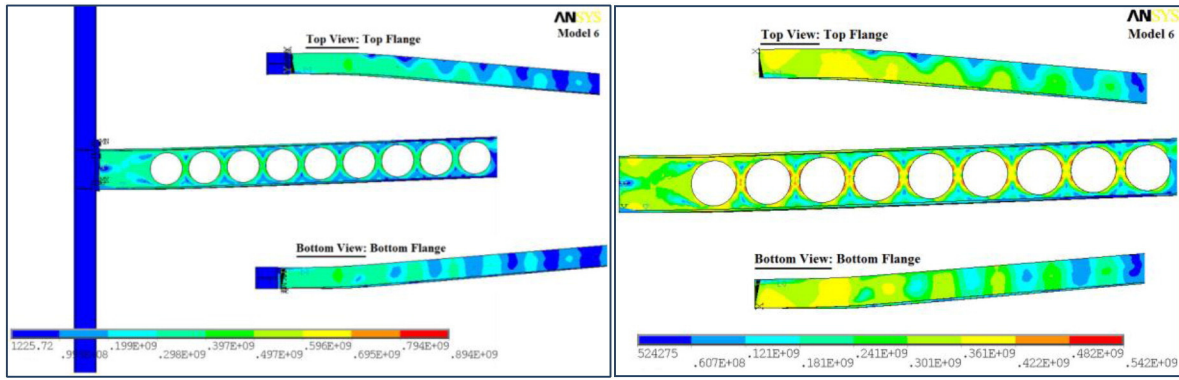
Fig. 29. Von-Mises stress contour plots of Model 6 (loading at 93.1 mm, cycle 27).

the first opening (approximately 300 MPa). The stresses in the bolts were also decreased to about 900 MPa. Therefore, Model 4 demonstrates a smooth stress distribution with low-stress intensity in the critical areas. In particular, the stress observed in the shear panel zone area was primarily triggered by the location of the first web opening being very close to the face of the column (S = 200 mm).

6.5.2. Model 5

Model 5 was developed based on the previous Model 4 while the column element was reinforced by introducing column stiffeners of thickness equal to that of the beam's flange thickness (10.8 mm). The FE Model 5 failed to converge at a later load-step 58 corresponding to cycle 29. Its hysteretic behaviour was plotted in Fig. 26.

Model 5 achieved an ultimate rotational capacity of 0.05 rad, compared to 0.015 rad for Model 4. The reduction of the maximum moment (93.75 kNm) was related to the lateral torsional buckling observed, while flanges were not being restrained. Model 5, however, presented increased ductility without strength degradation.

From Fig. 27, it can be concluded that the desired structural performance of RWS connections subjected to cyclic loading was finally achieved, while the stresses were predominately mobilised to the perforated beam away from the column shear panel zone and the connection.

In detail, stresses were mobilised towards the beam forming the so-called Vierendeel mechanism and the full formation of plastic hinges in the vicinity of the circular web openings. The shear panel zone of the

column as well as the end-plate experienced low stresses; the stress in the bolts decreased to about 890 MPa, which is not regarded as critical since grade 10.9 bolts with yield strength of 900 MPa were used. The end distance, S, resulted in high stresses of about 450 MPa when S = 200 mm and about 564 MPa when a closer distance to the end-plate was considered. At last, having a large web opening spacing following the first perforation reduced the stresses obtained from the next web openings.

6.5.3. Model 6

Model 6 was developed based on the latter Model 5, but an increased distance from the face of the column, S, equal to 520 mm was considered. The solution failed to converge at load-step 54 corresponding to cycle 27, hence a lower dissipated energy achieved. A lower maximum moment of 62.78 kNm than the previous Model 5 was achieved due to the earlier convergence. Regarding the ultimate rotational capacity, this model reached 0.04 rad which is also lower than the 0.05 rad achieved by Model 5. However, Fig. 28 shows a very ductile behaviour in the plastic region with strength degradation in the final cycle of about 3%.

An ideal behaviour of the connection was acquired while stresses concentrated in the beam at a satisfactory distance from the column face (Fig. 29). The stresses appeared in the low moment side of the first opening were further decreased to non-critical magnitudes. Hence, very low stress is found in the column shear panel zone and the end-plate as well as the bolts. Fig. 30 depicts the fully formed plastic
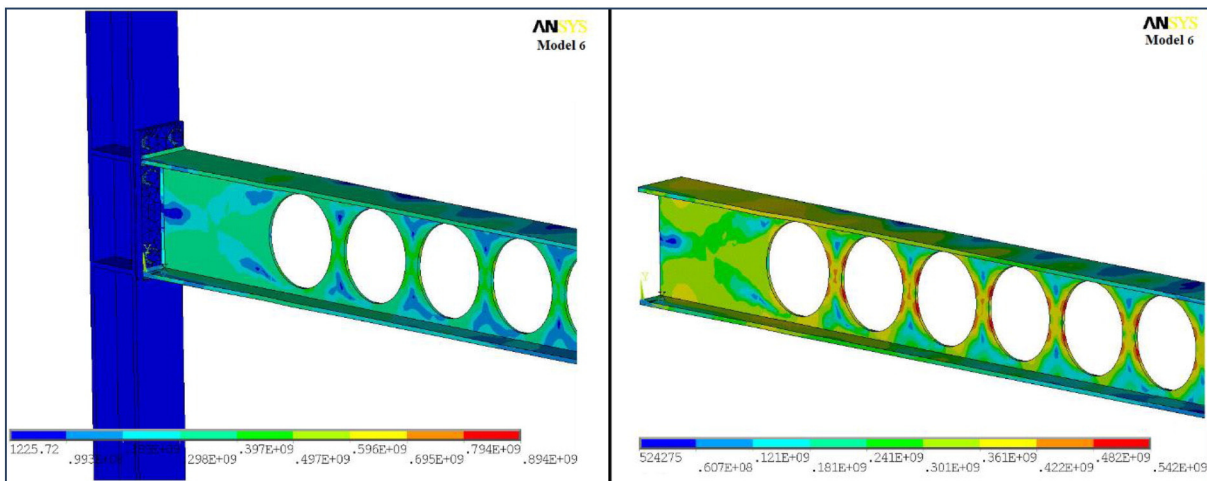

Fig. 30. Overall representation of stress distribution for Model 6 (loading at 93.1 mm, cycle 27).
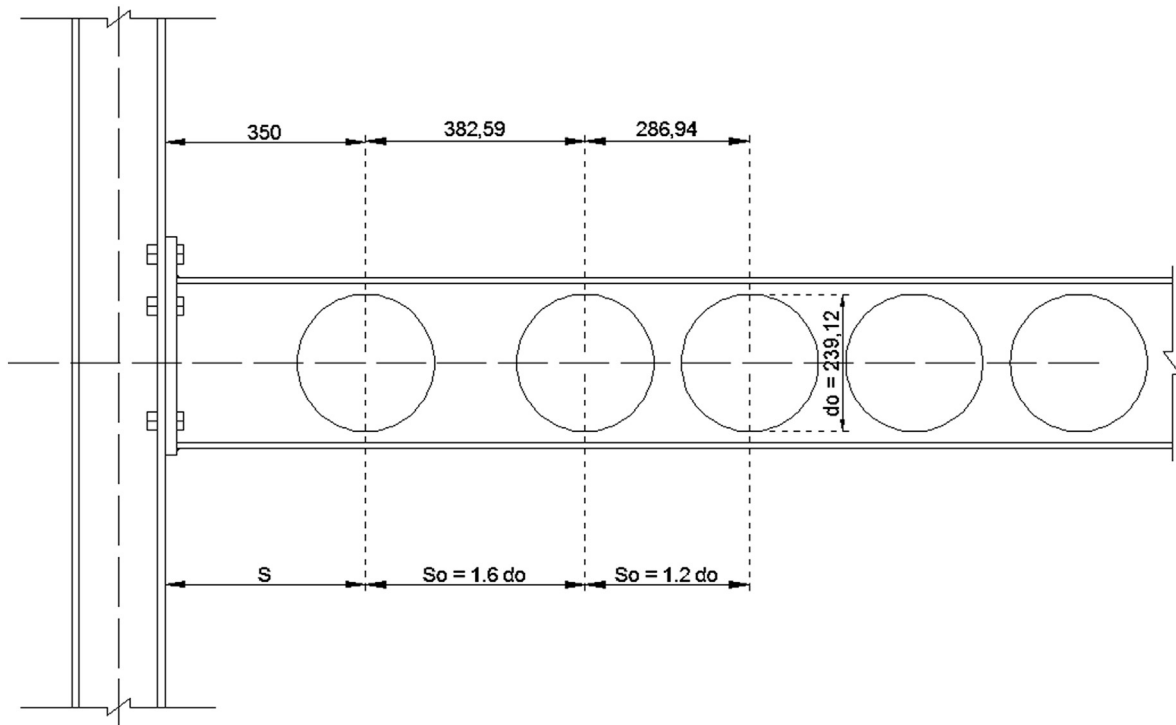
Fig. 31. Geometrical parameters of connection Model 7 (in mm).

hinges for every circular web opening at certain angles, and similar patterns along the length of the entire cellular beam. Consequently, containing a series of closely spaced web openings enables the stress to be transferred from the first web opening through the web-post to the adjacent web openings.

Local buckling was also observed in the final cycles, while it had an impact on the ultimate moment capacity reached by the connection. Model 6 achieved the best performance mobilising the stresses at a satisfactory distance from the critical areas. However, the hysteretic behaviour revealed lower ultimate rotational capacity and maximum moment in comparison with Model 5.

6.5.4. Model 7

In Model 7 the distance from the face of the column to the first web opening was increased from 200 mm to 350 mm (Fig. 31). The web opening spacing was changed to $S_o = 1.6d_o$ for the first two perforations, while no transfer of stresses anticipated, followed by closely spaced openings of $S_o = 1.2d_o$. The web opening depth is kept as equal to 0.8 h. For this specimen, the material properties as recorded in the experiment were used and column stiffeners were not utilised, similarly to models in Set 1.

The hysteretic behaviour was obtained in Fig. 32 and comparing Model 7 with Model 3, an almost identical behaviour was noticed. The
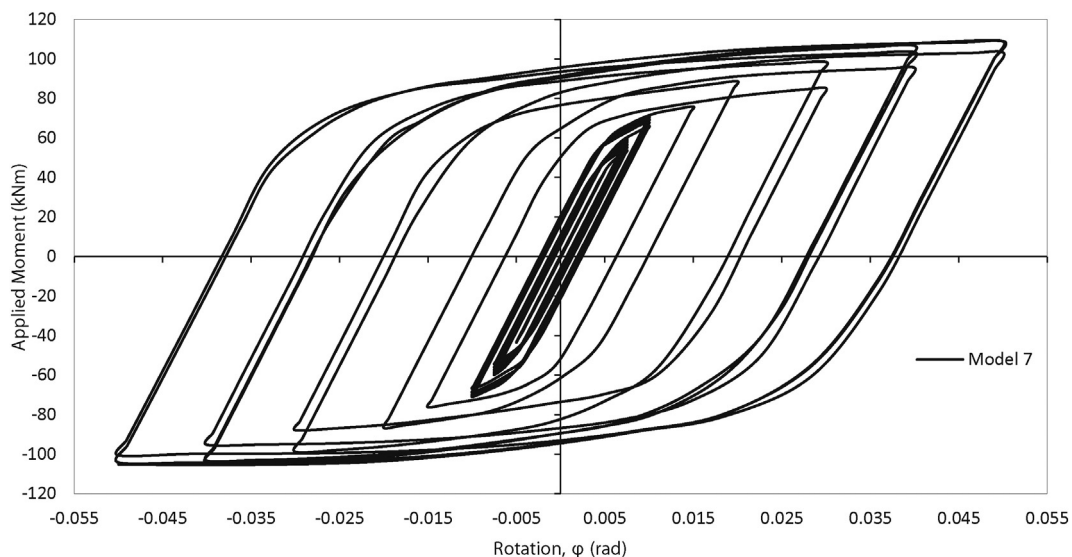

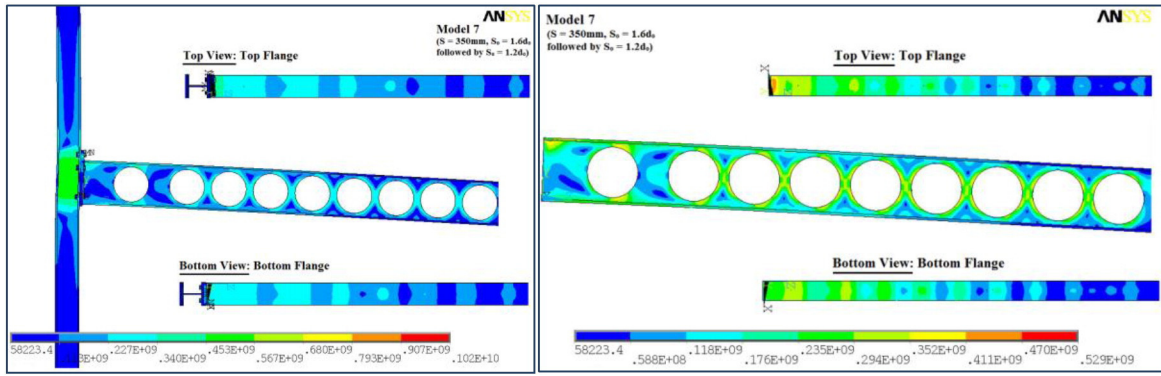Fig. 32. Hysteretic curve of Model 7 (S = 350 mm, $S_o = 1.6d_o$ followed by $S_o = 1.2d_o$).

Fig. 33. Von-Mises stress contour plots of Model 7 (loading at 155.1 mm, cycle 32).

same maximum ultimate rotation of 0.05 rad was achieved, while the ultimate moment was slightly increased to 108.94 kNm, as opposed to 105.77 kNm for Model 3. This is directly related to the same number of web openings utilised, and slightly affected by the increase of the end distance, S. The dissipated energy, E, recorded was equal to 124.23 (kNm) (rad), compared to 72.11 (kNm) (rad) for Model 3. The increase noted is significant, but still less than that of the specimen using the Solid beam Model (145.90 (kNm) (rad)).

From Fig. 33, it becomes apparent that high stresses are still concentrated in the critical panel zone of the column and similarly to Models 1 to 4; an ultimate strength of 450 MPa in panel zone and 1000 MPa at the top row bolts were recorded. The onset of plastic hinge formations for each opening took place at a lower stress level of about 350 MPa. It is worth noting that the increased web opening spacing between the first and second perforations resulted in high concentrated stresses which were not being transferred via the web-post.

6.5.5. Model 8

Fig. 34 represents the geometrical arrangement of Model 8 with S = 350 mm, $S_o = 1.6d_o$ followed by $S_o = 1.2d_o$ for the rest of the web-posts,

the use of nominal material properties (all S355 expect the bolts) as well as the addition of column stiffeners.

Model 8 failed to converge at load-step 58 corresponding to cycle 29. The hysteretic curve is presented in Fig. 35.

The hysteretic behaviour of Model 8 was similar to that of Model 7 in terms of the rotational ductility characteristics (i.e. initial loading line) as well as the ultimate rotational capacity with both models reaching 0.05 rad. Model 8 achieved a lower maximum moment of 96.02 kNm due to web buckling as opposed to 108.94 kNm recorded for Model 7.

As it was observed in Fig. 36, with the change to nominal material properties and the addition of column stiffeners, the "*weak beam-strong column*" mechanism was achieved. Stresses were mobilised to the beam promoting the Vierendeel mechanism. The shear panel zone of the column and the end-plate experienced low stress while the stress in the bolts decreased significantly to a maximum of about 850 MPa; below the f_y. The critical stresses were, therefore, located along the beam and not around the critical connection area. The wide end distance (S = 350 mm) resulted in high stresses of about 550 MPa to be concentrated away from the face of the column, avoiding to overstress the connection welds. However, when a large
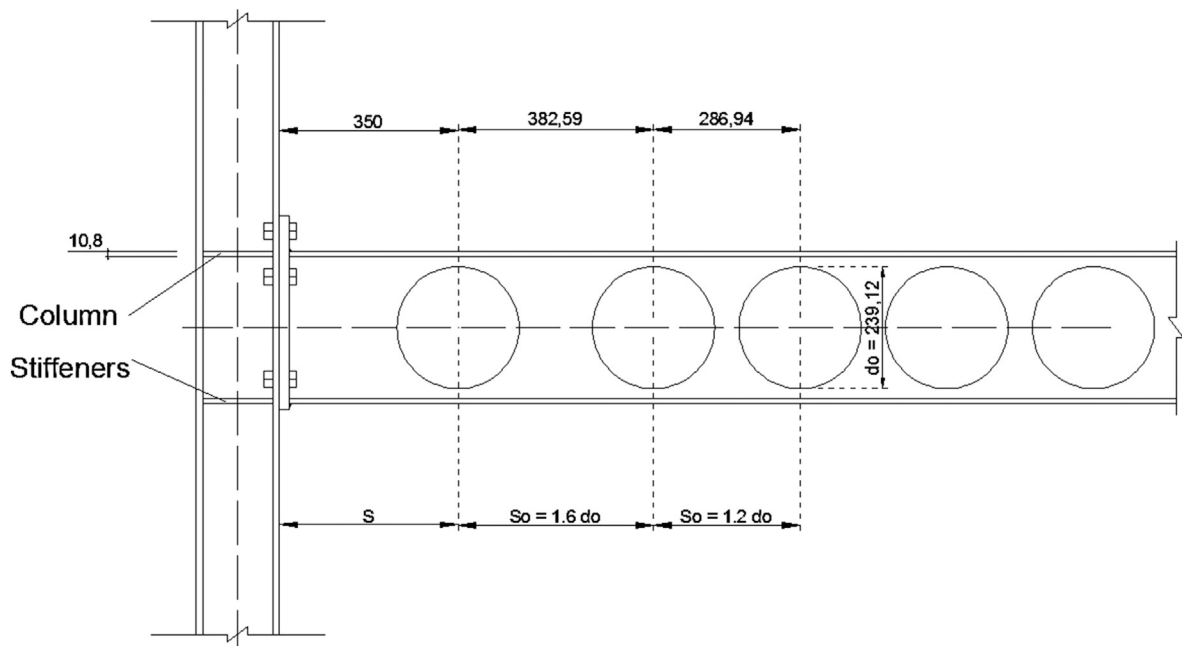

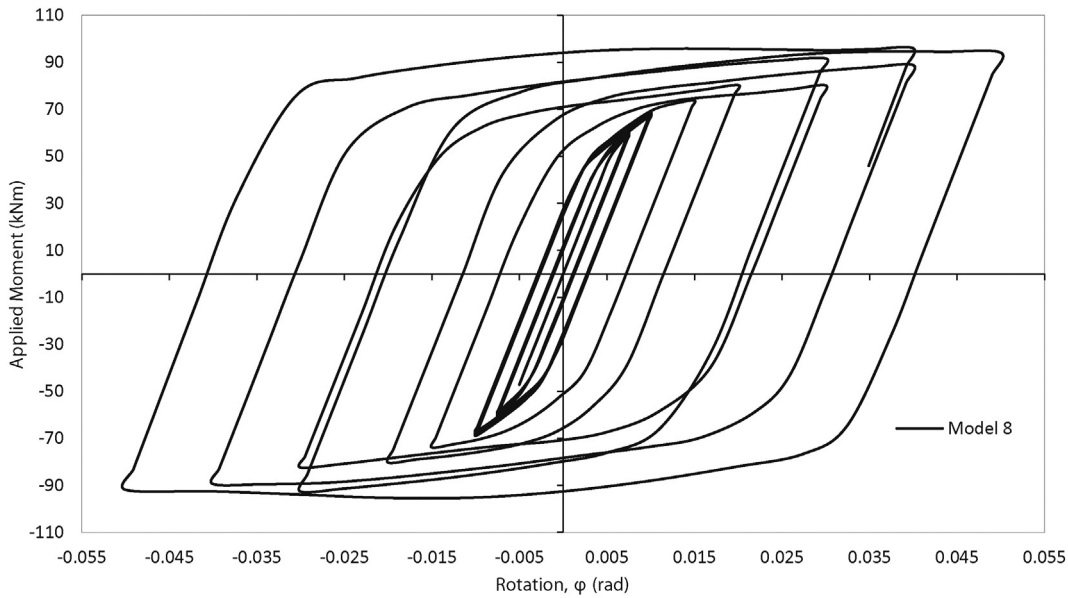**Fig. 34.** Geometrical parameters of connection Model 8 (in mm).

Fig. 35. Hysteretic curve of Model 8 (S = 350 mm, $S_o = 1.6d_o$ then $S_o = 1.2d_o$ with change in material properties and column stiffener).
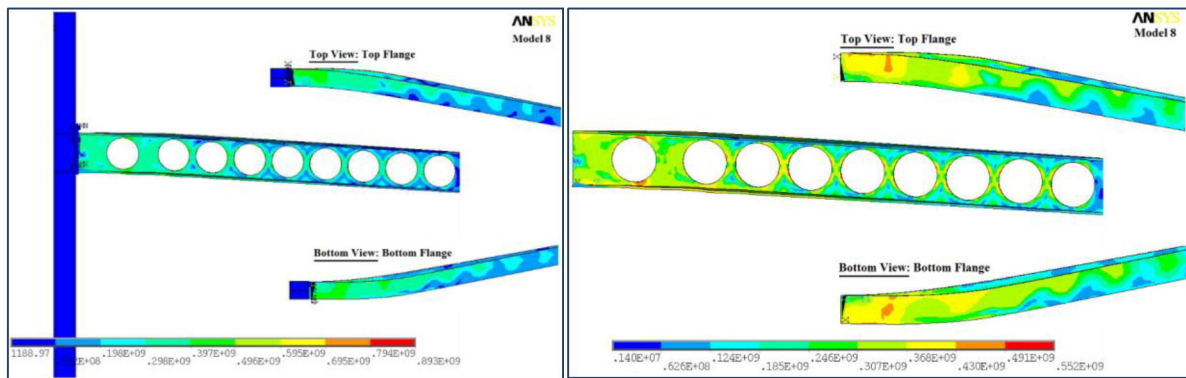

Fig. 36. Von-Mises stress contour plots of Model 8 (loading at 124.1 mm, cycle 29).

web opening spacing between the first and the second openings was used, further mobilisation of stresses along the length of the cellular beam was restricted. The results as recorded from Sets 2 and 3 are summarised in Table 6.

Table 6
Results summary table for Sets 2 and 3.

Specimen	Number of circular openings	Yield moment M_y (kNm)	Ultimate moment M_u (kNm)	Yield rotation φ_y (rad)	Ultimate rotation φ_u (rad)
Model 4	10	65.53	74.27	0.009993	0.014989
Model 5	10	58.59	93.75	0.00956	0.050000
Model 6	9	48.40	62.78	0.008562	0.040000
Model 7	9	59.41	108.94	0.008843	0.050034
Model 8	9	63.60	96.02	0.008562	0.050000

Specimen	Rotational ductility D_φ	Initial rotational stiffness K_i (kNm/rad)	Web opening area (mm²)	Dissipated energy E (kNm) (rad)
Model 4	1.50	8162.54	44,907.8	16.44
Model 5	5.23	7462.73	44,907.8	70.98
Model 6	4.67	7046.66	44,907.8	34.62
Model 7	5.66	8771.68	44,907.8	124.23
Model 8	5.84	9435.23	44,907.8	71.60

6.6. Results: Set 4 (Models 9, 10 and 11)

All models in Set 4 are consisted by fully perforated cellular beams, with nominal material properties as well as column stiffeners. All three models have closely spaced web openings to be able to transfer the stresses to the adjacent openings. The flanges have been restrained on the z-axis transverse to the web to simulate the presence of the composite slabs. Three distances, S, were examined: 200 mm, 350 mm and 520 mm. The hysteretic behaviours from all models in Set 4 were plotted in Fig. 37.

6.6.1. Model 9

Model 9 achieved all 64 load-steps corresponding to the 32 cycles. It reached an ultimate rotational capacity of 0.05 rad, as seen previously with models having S = 200 mm. Also, it reached a higher maximum moment of 128.51 kNm.

It is worth to note that with the change in material properties and the addition of column stiffeners, the 'weak beam-strong column' mechanism was achieved. Also, since the flanges are restrained, the beam is not experiencing any out-of-plane movement, hence the high maximum moment capacity. In practice, the composite slab is providing such lateral restraint, hence the models in Set 4 are more representative. In detail, the stresses were mobilised to the beam forming the
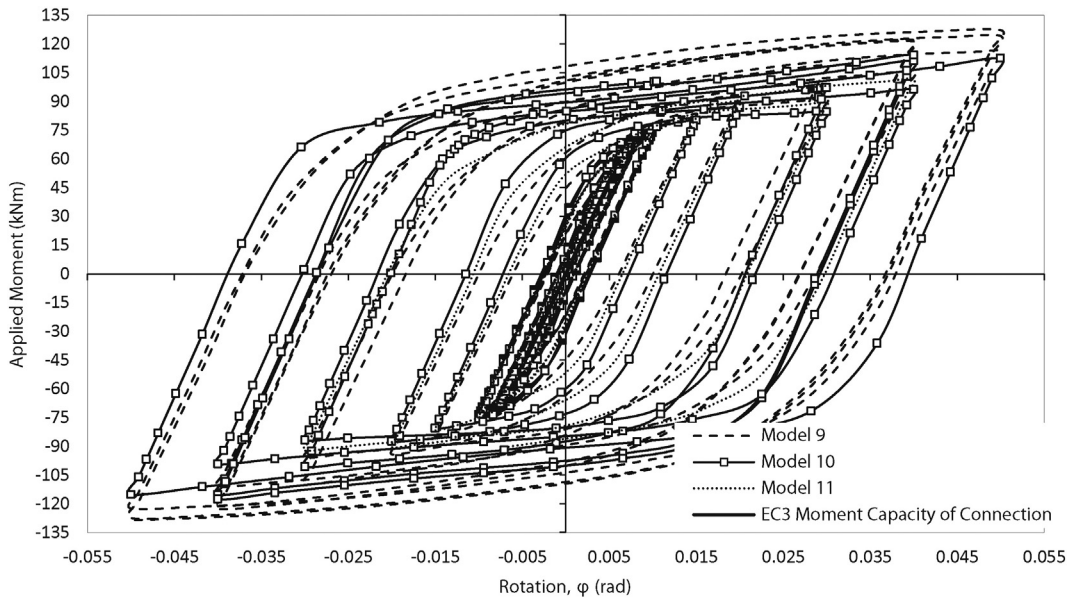
Fig. 37. Moment–rotation curves of FE Set 4.

Vierendeel mechanism, and the formation of plastic hinges in the vicinity of circular openings was visible. The column shear panel zone, as well as the end-plate experienced low intensity stresses, and the stress in the bolts decreased significantly to a maximum of about 850 MPa. Moreover, the closely spaced web openings resulted in an adequate transition of stresses over the adjacent web openings. The critical stresses of 565 MPa were found along the beam. However, some high stresses remained in the vicinity of the welds as it is shown in Fig. 38. The distance S = 200 mm is deemed to be narrow to mobilise the stresses away enough from the face of the column.
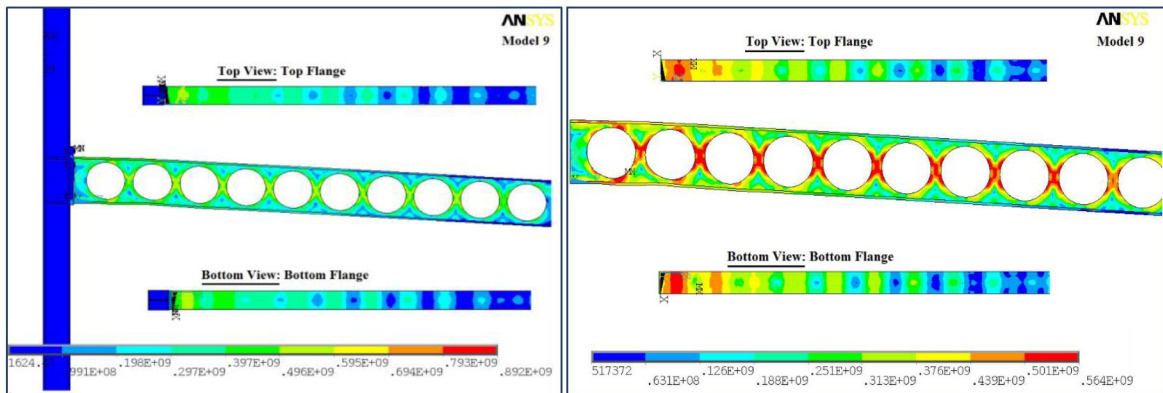

Fig. 38. Von-Mises stress contour plots of Model 9 (loading at 155.1 mm, cycle 32).
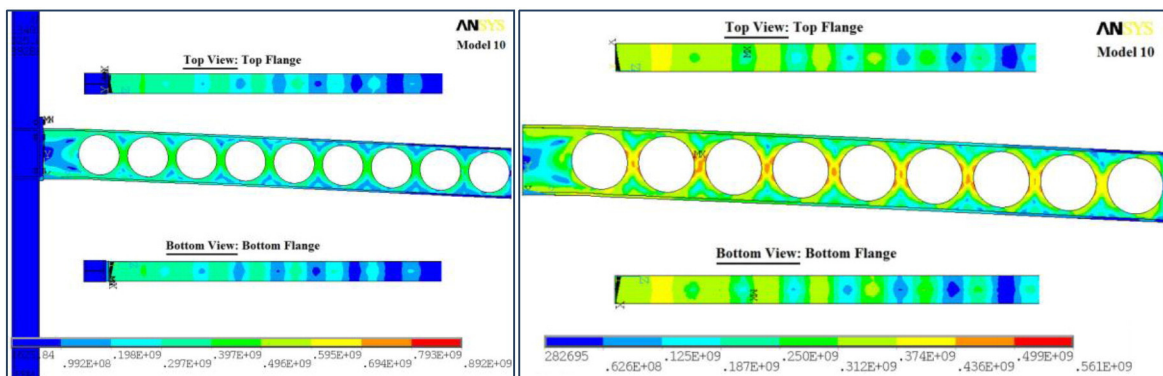

Fig. 39. Von-Mises stress contour plots of Model 10 (loading at 155.1 mm, cycle 31).
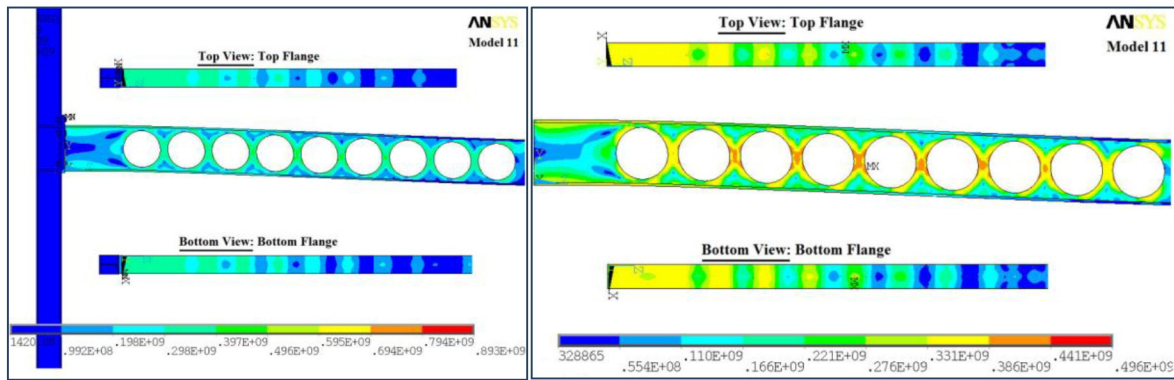
Fig. 40. Von-Mises stress contour plots of Model 11 (loading at 62.1 mm, cycle 36).

6.6.2. Model 10

Model 10 failed to converge at load-step 61 corresponding to cycle 31. However, the ultimate rotational capacity of 0.05 rad was achieved, as seen previously with models having S = 350 mm and achieved a higher maximum moment capacity compared to the previous models while using the same end distance, S, of 117.56 kNm. Regarding the stress distribution (Fig. 39), the changes followed in Model 10 resulted its improved structural behaviour in comparison to Model 9.

The desired mechanism was achieved while lateral torsional buckling was recorded in higher moment. The column web panel zone as well as the end-plate experienced little to no stress; the stress in the bolts decreased significantly to a maximum of about 850 MPa. The critical stresses of 560 MPa were found along the beam, with only some stress in the vicinity of the welds, as compared to Model 9. The dimension S = 350 mm is deemed to be ideal to mobilise the critical zone away from the face of the column and achieve enhanced structural performance.

6.6.3. Model 11

Model 11 failed to converge at load-step 52 corresponding to cycle 26 and because of this, it achieved an ultimate rotational capacity of only 0.04 rad, similarly to models with S = 520 mm. Model 11 also attained a higher maximum moment than previous models using the same distance from the face of the column, of 101.65 kNm. It is concluded that the changes made in Model 11 resulted in a very similar behaviour to Model 10 (Fig. 40).

The shear panel zone and the column experienced low-stress levels, and the stress in the bolts decreased significantly to a maximum of about 850 MPa. The critical zone (approximately 500 MPa) is found along the beam, with very low stresses in the vicinity of the welds. The end distance, S, equal to 500 mm is deemed to be also capable to mobilise the critical stresses away from the face of the column, but an ultimate rotational capacity of 0.04 rad compared to 0.05 rad for S = 350 mm is now achieved due to other computational issues. The results of Set 4 are summarised in Table 7.

7. Concluding remarks and limitations

This paper presents a comprehensive FE parametric study introducing extended end-plate beam-to-column connections with cellular beams subjected to cyclic loading. It is essential for the connection to be sufficiently strong and robust, mobilising the stresses to a desired location along the length of the beam away from the connection assembly, creating the "*weak beam-strong column*" mechanism through the formation of plastic hinges proving the performance of RWS connections with cellular beams to be used in seismic-resistant designs.

It is concluded that such connections behave in a satisfactory manner and provide an ideal structural behaviour in terms of stress distribution when subjected to cyclic loading, especially when the first web opening is located at a particular distance from the face of the column. Cellular beams with nominal material properties are also examined (S355 for all components and bolts with Class 10.9), as the initial difference in material properties taken from the tests hindered the desired mechanism. The addition of column stiffeners as well as the use of restraints on the beam flanges, similarly to the practice, was also investigated. Both specimens with either closely ($S_o = 1.2d_o$) or widely ($S_o = 1.6d_o$) spaced web openings showed positive results, with the latter ones mobilised the critical stresses mainly in the vicinity of the first web opening.

The critical distance, S, of 520 mm for the first web opening resulted in the decrease of the ultimate rotational capacity from 0.05 rad to 0.04 rad (Model 6 and 11) due to early ending of the FE analysis, while the narrow distance of 200 mm leads to critical stress concentration close to the column face. The ideal end distance, S, was therefore identified as being 350 mm (i.e. $S = 1.2d_o$ - the diameter of the opening is approximately equal to the 96% of the beam depth).

It is suggested that a wide range of section properties of the connected members as well as web opening shapes should be studied in the future to be able to non-dimensionalize the results and reveal the influence of all geometric parameters onto the performance of RWS connections with cellular beams. Having identified some critical geometric parameters and their influence to the behaviour of such

Table 7
Results summary table for Set 4.

Specimen	Number of circular openings	Yield moment M_y (kNm)	Ultimate moment M_u (kNm)	Yield rotation φ_y (rad)	Ultimate rotation φ_u (rad)
Model 9	10	69.7	128.51	0.009600	0.050000
Model 10	9	67.5	117.56	0.007450	0.050000
Model 11	9	64.40	101.65	0.007500	0.040000

Specimen	Rotational ductility D_φ	Initial rotational stiffness K_i (kNm/rad)	Web opening area (mm²)	Dissipated energy E (kNm) (rad)
Model 9	5.21	9400.30	44,907.8	135.80
Model 10	6.71	10,309.41	44,907.8	101.76
Model 11	5.33	9666.92	44,907.8	40.12

connections, the appropriate design analogies should be examined for certain commonly-used seismic-resistant connections of steel structures.

References

[1] Eurocode 3, Design of Steel Structures — Part 1: General Rules and Rules for Buildings, EN 1993-1-1, Brussels, Belgium, 2005.
[2] Eurocode 8, Part 3: Design of Structures for Earthquake Resistance. Assessment and Retrofitting of Buildings. EN 1998-3, June 2005.
[3] FEMA 350, Recommended Seismic Design Criteria for the New Steel Moment Frame Buildings, Report No. FEMA 350, SAC Joint Venture, CA, 2000.
[4] D. Pachoumis, E. Galoussis, C. Kalfas, A. Christitsas, Reduced beam section moment connections subjected to cyclic loading: experimental analysis and FEM simulation, Eng. Struct. 31 (2009) 216–223.
[5] E. Brunesi, R. Nascimbene, G.A. Rassati, Evaluation of the response of partially restrained bolted beam-to-column connection subjected to cyclic pseudo-static loads, Proceedings of the Structures Congress 2013: May 2–4, 2013, American Society of Civil Engineers, Pittsburgh, Pennsylvania, 2013.
[6] E.P. Popov, T.-S. Yang, S.-P. Chang, Design of steel MRF connections before and after 1994 Northridge earthquake, Eng. Struct. 20 (1998) 1030–1038.
[7] C.W. Roeder, Connection performance for seismic design of steel moment frames, J. Struct. Eng. 128 (2002) 517.
[8] C. Lee, J. Kim, Seismic design of reduced beam section steel moment connections with bolted web attachment, J. Constr. Steel Res. 63 (2007) 522–531.
[9] M. Kazemi, A. Hosseinzadeh, Modelling of inelastic mixed hinge and its application in analysis of the frames with reduced beam section, Int. J. Steel Struct. 11 (1) (2011) 51–63.
[10] G.S. Prinz, P.W. Richards, Eccentrically braced frame links with reduced web sections, J. Constr. Steel Res. 65 (2009) 1971–1978.
[11] Q. Yang, B. Li, N. Yang, Aseismic behaviors of steel moment resisting frames with opening in beam web, J. Constr. Steel Res. 65 (2009) 1323–1336.
[12] A.A. Hedayat, M. Celikag, Post-Northridge connection with modified beam end configuration to enhance strength and ductility, J. Constr. Steel Res. 65 (2009) 1413–1430.
[13] K.D. Tsavdaridis, F. Faghih, N. Nikitas, Assessment of perforated steel beam-to-column connections subjected to cyclic loading, J. Earthq. Eng. 18 (8) (2014) 1302–1325.
[14] K.D. Tsavdaridis, C. D'Mello, Finite Element Investigation on Web-post Buckling of Perforated Steel Beams with Various Web Opening Shapes Subjected Under Different Shear-Moment Interaction, EUROSTEEL, 2011 (Available from: http://openaccess.city.ac.uk/).
[15] K.D. Tsavdaridis, C. D'Mello, Web buckling study of the behaviour and strength of perforated steel beams with different novel web opening shapes, J. Constr. Steel Res. 67 (2011) 1605–1620.
[16] K.D. Tsavdaridis, C. D'Mello, Vierendeel bending study of perforated steel beams with various novel web opening shapes through nonlinear finite-element analyses, J. Struct. Eng. ASCE 138 (2012) 1214–1230.
[17] K.D. Tsavdaridis, C. D'Mello, Optimisation of novel elliptically-based web opening shapes of perforated steel beams, J. Constr. Steel Res. 76 (2012) 39–53.
[18] K.D. Tsavdaridis, C. Pilbin, Finite element modelling of steel connections with web openings: aseismic design and avoidance of progressive collapse, The 7th European Conference on Steel and Composite Structures, Eurosteel. 10–12 September, Napoli, Italy, 2014.
[19] S. Wilkinson, G. Hurdman, A. Crowther, A moment resisting connection for earthquake resistant structures, J. Constr. Steel Res. 62 (2006) 295–302.
[20] R. Hamburger, A. Whittaker, Design of steel structures for blast-related progressive collapse resistance, Mod. Steel Constr. 44 (2004) 45–58.
[21] ANSYS, Release 14.0, ANSYS, Inc., Canonsburg, PA., 2011
[22] C. Díaz, M. Victoria, P. Marti, O. Querin, FE model of beam-to-column extended end-plate joints, J. Constr. Steel Res. 67 (2011) 1578–1590.
[23] J. Janss, J.P. Jaspart, R. Maquooi, Appl. Sci. Elsevier 1987, pp. 26–32.
[24] Y. Maggi, R. Gonçalves, R. Leon, L. Ribeiro, Parametric analysis of steel bolted end plate connections using finite element modeling, J. Constr. Steel Res. 61 (2005) 689–708.
[25] C. Díaz, P. Marti, M. Victoria, Diseño optimo de uniones semirrígidas mediante simulación numérica y modelos krigingOnline, Accessed 10 December 2013, Available from: http://hdl.handle.net/10317/14702010.
[26] O.S. Bursi, J.P. Jaspart, Calibration of a finite element for isolated bolted end plate steel connections, J. Constr. Steel Res. 44 (1997) 225–262.
[27] A.M. Girão Coelho, F.S.K. Bijlaard, Experimental behaviour of high strength steel end-plate connections, J. Constr. Steel Res. 63 (2007) 1228–1240.
[28] N. Largaros, D.L. Psarras, M. Papadrakakis, G.S. Panagiotou, Optimum design of steel structures with web openings, Eng. Struct. 30 (9) (2008) 2528–2537.